A mathematical model to investigate the key drivers of the biogeography of the colon microbiota.

Simon Labarthe, Bastien Polizzi, Thuy Phan, Thierry Goudon, Magali Ribot, Béatrice Laroche

A mathematical model to investigate the key drivers of the biogeography of the colon microbiota.

Simon Labarthe [1,*],Bastien Polizzi [2], Thuy Phan [3], Thierry Goudon [4], Magali Ribot [3], Beatrice Laroche [1],
1 MaIAGE, INRA, Paris-Saclay University, Jouy-en-Josas, France

2 IMFT, CNRS-INPT-Paul Sabatier University, Toulouse, FRANCE,
3 IDP, Université d'Orléans-CNRS, Orleans, FRANCE
4 Université Côte d'Azur, Inria, CNRS, LJAD, Nice, FRANCE

* Current Address: MaIAGE, INRA, Université Paris-Saclay, 78350 Jouy-en-Josas, France, Jouy-en-Josas
simon.labarthe@inra.fr

Abstract

The gut microbiota is engaged in a complex dialogue with the large intestinal epithelium through which important regulatory processes for the health and well-being of the host take place. Imbalances of the microbial populations, called dysbiosis, are related to several pathological status, emphasizing the importance of understanding the gut bacterial ecology. Among the ecological drivers of the microbiota, the spatial structure of the gut is of special interest: spatio-temporal mechanisms can lead to the constitution of spatial interactions among the bacterial populations and of environemental niches that impact the overall colonization of the gut. In the present study, we introduce a mathematical model of the gut microbiota in its fluid environment, based on the explicit coupling of a population dynamics model of microbial populations involved in fibre degradation with a fluid dynamics model of the gut content. This modelling framework is used to study the main drivers of the spatial structure of the microbiota, specially focusing on the dietary fibres, the epithelial motility, the microbial active swimming and viscosity gradients in the digestive track. We found 1) that the viscosity gradients allow the creation of favourable niches in the vicinity of the mucus layer; 2) that very low microbial active swimming in the radial direction is enough to promote bacterial growth, which shed a new light on microbial motility in the gut and 3) that dietary fibres are the main driver of the spatial structure of the microbiota in the transverse and distal bowel whereas epithelial motility is preponderant for the colonization of the proximal colon.

1 Introduction

Humans host in their gut a large community of symbiotic microorganisms: the gut microbiota. Complex ecological cross-talks between the microbial populations and the gut epithelium are involved in the regulation of this community, but also in the host homeostasis [**?**]. Microbial population imbalances, called

dysbiosis, are now associated with number of physiopathological status, such as metabolic, auto-immune, inflammatory or even mental diseases[**?**, **?**]. The microbial ecology of the gut is thus intensively studied in order to better understand the link between the gut microbiota and the host health and wellness by deciphering the mechanisms that shape the microbiota community structure.

Among them, the spatial organization of the microbiota plays an important role, both in the installation and maintenance of the microbiota, and impacts the host health, as recently outlined in [**?**]. The identification of the parameters that influence this spatial structure is of particular interest.

First, the gut is the place of complex fluid mechanics: the luminal flow of digestive residuals carries along the gut content towards its distal part, while the gut epithelium pumps water [**?**], twisting the stream lines and reducing the transport speed. In the same time, the mucus layer that wraps the epithelium, together with the inhomogeneous gut content, creates viscosity gradients that further deform the flow [**?**] while the active contractions of the gut wall during its motile activity [**?**] induce additional perturbations. These interacting hydrodynamic and mechanic forces spatio-temporally structure the gut microbiota.

The second parameter impacting the spatial distribution of the microbiota is the nutrient availability. The gut is an anaerobic medium, where the main nutrient sources for microorganisms are undigested dietary fibres or host-derived polysaccharides and their by-products: this constitutes a selection pressure that favors fermentative microorganisms. The polysaccharides degradation is therefore central in the ecological interactions within the microbiota and structures the whole community through trophic exchanges of electron acceptors[**?**]. The interplay between the microbial populations and their nutritional landscape can be further intricate due to their ability to forage for nutritional sources through active motion: whereas bacterial flagela expression is repressed by the host immune system near the epithelium [**?**], active swimming is needed for the colonization of several pathogens [**?**] and low motile activity is observed for commensal bacteria [**?**].

Finally, the epithelial mucus plays a particular role in the gut microbiota homeostasis and its spatial shape. This viscous fluid insulates the epithelium wall and forms a passive protection against a microbial invasion. But it also provides an additional way for the bacteria to escape the flow of the intestinal content by binding to the mucus layer to prevent their wash out. Furthermore, the mucus represents a source of polysaccharides directly provided by the host: the mucins and their glycans that compose the epithelial mucus can be degraded with the same enzymatic mechanisms than for fibres [**?**].

Experimental devices mimicking the gut environment provide highly valuable information [**?**, **?**, **?**, **?**, **?**] on the gut microbiota functioning and its spatial structure. Reductionist approaches on gnotobiotic rodents [**?**] are also highly valuable tools. However, they only partialy mimic the host response or the ecosystem functions, making it difficult to evaluate the relative importance of the factors that shape the spatial distribution of the microbiota. This is why mathematical modelling approaches provide a helpful complement to experiments to gain insight on the main parameters influencing the spatial structure of the bacteria in the gut.

Several models of the gut microbiota were proposed in the literature to study the spatial structure of the microbial communities. The first model that was introduced [**?**] emphasized the modelling of the fibre degradation activity, by

adapting a model of anaerobic digestion from bioprocess engineering [?]. The space was handled through a rough discretization of the colon into physiological compartments. An improved version of this model, based on an infinite sequence of longitudinal compartments represented by a one-dimensional partial differential equation was developed in [?]. It assumed a constant flow speed along the gut, reducing the fluid mechanic effects to an averaged retention time. A more sophisticated description of the hydrodynamic transport speed was proposed in [?], together with a diffusive term describing the peristaltic activity of the large intestine assessed by comparison with biophysical experiments [?], and a pH-dependant bacterial activity. The resulting model was unidimensional in space, and the hydrodynamics was reduced to the volume conservation during water absorption, while the gut microbial community was simplified up to a pair of bacterial strains. In [?], an accurate description of the fluid dynamics of the multiphasic gut content was proposed to study the constitution and the turnover of the mucus layer, but the interactions with the microbiota were not studied.

In this paper, we present a new model coupling the fluid mechanics model of the gut content and the mucus layer introduced in [?] with the metabolic model of bacterial populations presented in [?]. To our knowledge, this model allows for the first time a full study of the spatial distribution of the microbiota including the interactions with its fluid environment. The complexification of the fluid mechanics description allowed to investigate specific features such as epithelial motility, active swimming or the dependency of the local viscosity to the gut content composition, together with their impact on the fluid streams and the microbiota growth.

2 Results

We first present our model in subsection 2.1. Then, we define a reference state reproducing the results introduced in [?] and [?]: we knock down the bacterial active motion and the gut motility, that were not considered in these studies, to recover the main characteristics of the gut microbiota (subsection 2.2). This numerical experiment is subsequently used as a reference control to assess the effect of different mechanisms on the gut spatial structure: diet variations (subsection 2.3.1), viscosity gradient and mucus metabolisms (subsection 2.3.2), peristaltism and active motion (subsection 2.3.3). We finally compare the relative influence of each mechanism in the multifactorial process leading to the spatial structuration of the gut (subsection 2.3.4) through a sensitivity analysis of the model.

2.1 A spatialized mathematical model of the gut microbiota in its environment

We built a mathematical model of the gut microbiota dynamics, with a focus on the interactions with its fluidic environment. This model couples the population dynamics of the bacterial communities and the evolution of the fluidic luminal content, and gathers the main mechanisms that drive its spatial structuration (see Fig. 1 for a synthetic view of the different processes included in the model). It is formulated as a set of partial differential equations (PDE) the

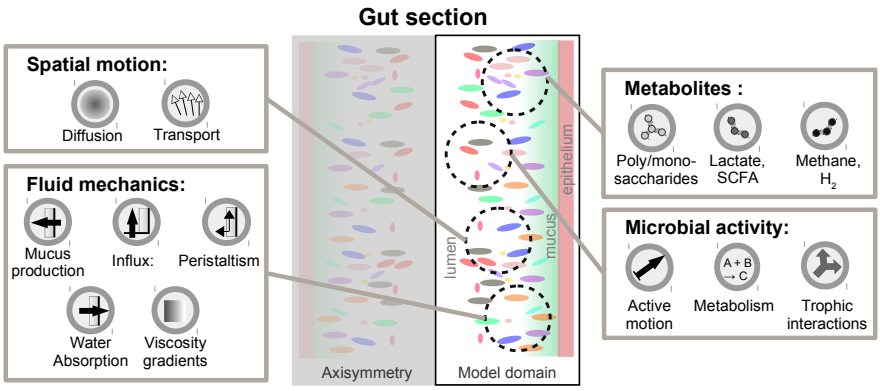

Figure 1: Overview of the different processes considered in the model.

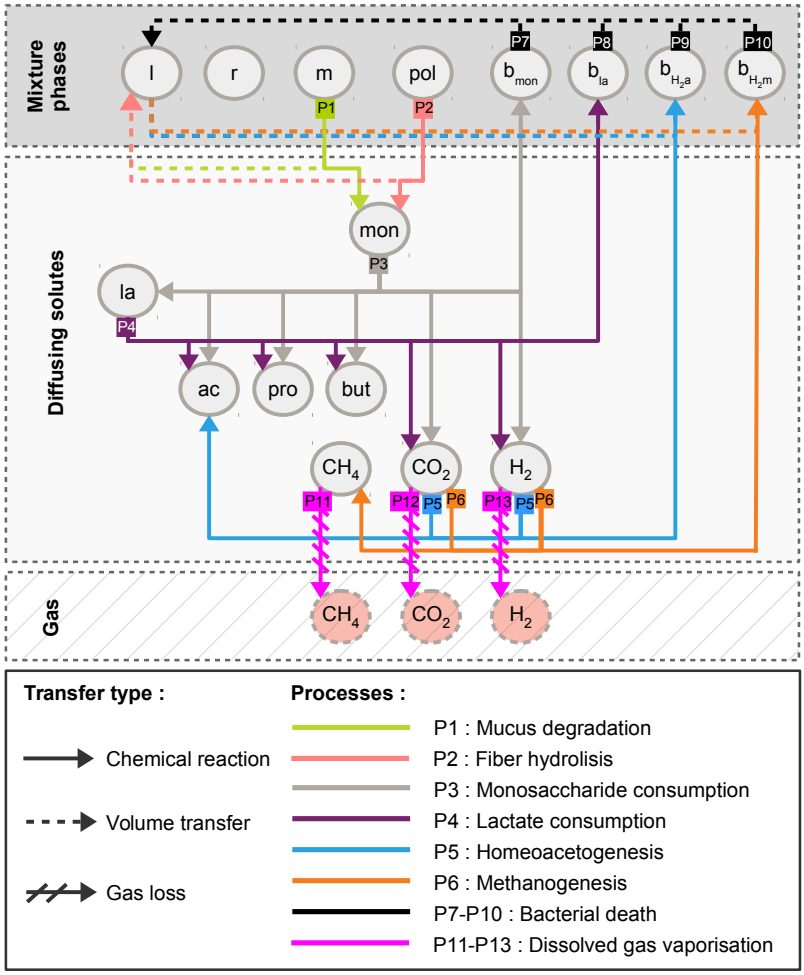

Figure 2: Graph of the reactions and volume transfers considered in the model

detailed formulation of which is provided in the Material and Methods (section 3). The geometry of the gut is considered as a cylinder with physiological dimensions and the usual segmentation of the colon in proximal, transverse and distal compartments is used at the post-processing phase, in order to compare the model outputs with previous numerical or experimental data. We note that we do not consider the final part of the colon, which would necessitate a more accurate description of the intestinal emptying after defecation: the end of the sigmoid segment is then not modelled. The geometrical characteristics of the model are gathered in Table 1.

Following [**?**], the bacterial interactions in the microbiota are drastically simplified by only considering trophic interactions involved in the fibre degradation pathways, which is the main substrate available in the gut. This model structure relies on the prior knowledge of the anaerobic fibre degradation, representing through functional populations the main degradation processes. The microbial communities are clustered in four functional populations: the poly and monosaccharides consumers (population 1), the lactate consumers (population 2), the hydrogen consumers producing acetate (population 3) or methane (population 4). We also model the key metabolites involved in fibre degradation: polysaccharide (fibres) and monosaccharides, lactate, short chain fatty acids (SCFA), gas (methane, CO2, H2) and non-digestible residuals (see Fig. 2 for a synthetic view of the model structure and of the different metabolic processes). A linear increasing pH is applied along the gut, mainly impacting methanogens [**?**]. The dynamics of each bacterial and metabolite population is governed by a mass-conservation reaction-diffusion-convection PDE: the diffusive and convective parts of the equation model the transport of the bacteria by brownian motion, carriage by the fluidic environment or active swimming, while the reaction part accounts for the bacterial metabolism and the trophic interactions. The PDEs allow for a continuous description of the 3D dynamics of the bacteria in the gut at the millimeter scale, making available accurate description of both the longitudinal and radial structures of the bacterial communities.

The dynamics of the fluid gut content is described with a mixture model [**?**, **?**, **?**] of multi-phasic flows. This modelling method is flexible enough to deal with all the main physiologic mechanisms that shape the fluid flow in the gut: water inflow, water absorption by the epithelium, viscosity gradients all along the gut, mucus production and peristaltism. The complex numerical resolution of the mixture model is avoided by the introduction of an approximate asymptotic model with an explicit solution: the 3D velocity field of the gut content is computed with a comprehensive formula that includes the main drivers of the flow. This simple expression of the fluid dynamics allows to knock out or modulate the different mechanisms in order to study their relative influence on the overall spatial structure of the microbiota. We note that we do not consider periodic features such as post-prendrial influx or defecation: a more detailed modelling of the fluid mechanics should be introduced to integrate these features.

2.2 Characterisation of the reference state

We aim at studying the mechanisms that drive the spatial structure of the gut microbiota at equilibrium. We thus need to characterize a correct proxy of the homoeostatic state of the gut microbiota. Starting from a colon with liquid

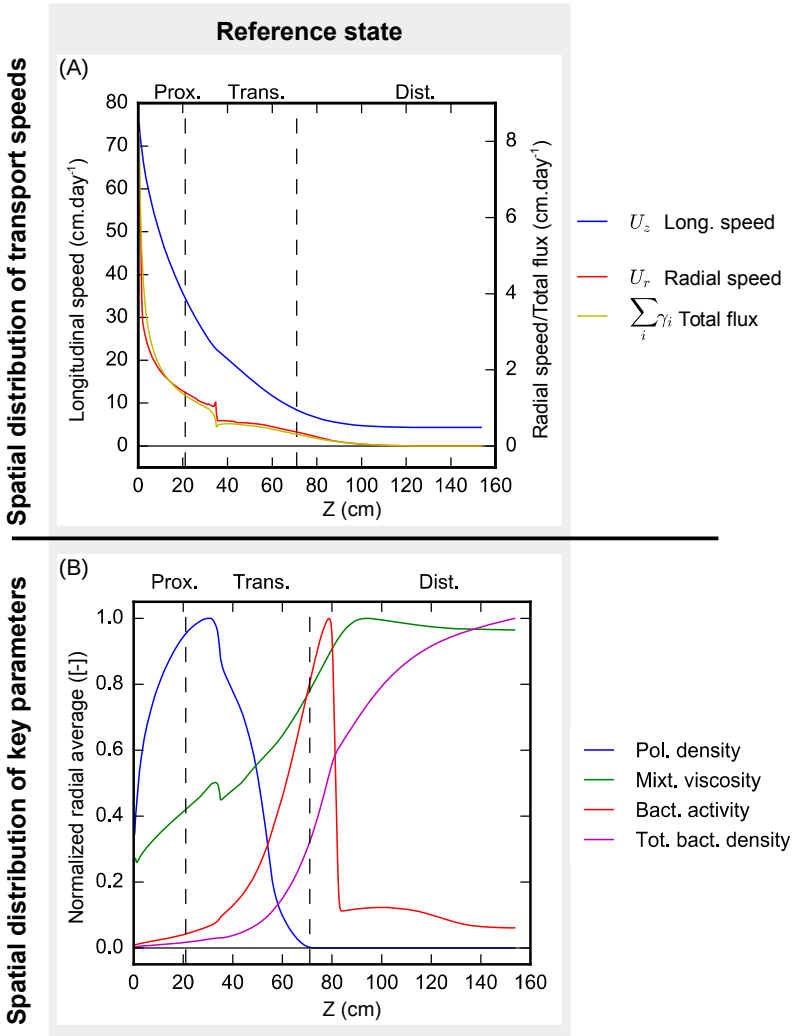

Figure 3: Transport speeds and key parameters of the spatial structure. (A) The longitudinal distribution of the radially averaged radial ($U_r(z) := \frac{2}{R^2}\int_0^R r u_{s,r}(r,z)dr$) and longitudinal speeds ($U_z(z) := \frac{2}{R^2}\int_0^R r u_{s,z}(r,z)dr$), together with the total flux of water and mucus through the mucosa ($\sum_i \gamma_i$), are displayed. We indicate by dashed lines the position of longitudinal compartments that are considered for observation issues: proximal, transverse and distal colon. In the lower panel, the averaged value of key parameters along the gut is presented. The different quantities are normalized by their maximal value to allow representation in the same graph. The maximal values of polysaccharide density, mixture viscosity, microbial functionnal activity and total microbial density are respectively $6.74e-2$, $3.88e3 \mathrm{g\,cm^{-1}\,d^{-1}}$, $8.34e-3 \mathrm{d^{-1}}$ and $6.10e-2$.

and mucus only, we perform a long term simulation of our PDE model until steady state, with normal microbial and metabolite influx and discarding motile activity of the gut wall or bacterial active swimming. We first assess that this equilibrium, defined as the reference state, correctly reproduces physiological markers of the structure and function of a healthy microbiota in the colon.

2.2.1 Longitudinal structure of the colon in the reference state.

The longitudinal distribution of several parameters driving the fluid mechanics and the overall microbial steady-state levels are displayed in Fig. 3. We can see (Fig 3 A) that the averaged longitudinal speed decreases strongly in the proximal and transverse sections, where the pumping activity by the mucosa is maximal. It then reaches an average speed of $4.03\text{cm}\,\text{d}^{-1}$, which corresponds to a outgoing flux of $169\text{mL}\,\text{d}^{-1}$, in the range of natural water excretion in faeces (100-200mL d^{-1} [**?**]). The radial speed reaches its highest level at the beginning of the gut and then drops off in the distal gut to negligeable values. The radial transport is thus expected to dominate over the radial diffusive process in the proximal colon, while the dominance ratio is reversed distally. The curve of the averaged radial speed (red curve, Fig 3-A) nearly overlaps the curve of the total fluxes through the mucosa (yellow curve, Fig 3-A). A key parameter for the speed dynamics is the viscosity distribution. We can observe (green curve, Fig 3-B) that the viscosity of the gut mixture increases all along the colon until reaching a maximal value in its distal part before a slight decrease, due to mucus consumption by the microbiota. The viscosity increase reflects water absorption and the resulting concentration of the other mixture components. The microbial growth (red curve, Fig 3-B) is mostly driven by the polysaccharides metabolism. The fibres start accumulating in the proximal colon, under the effect of a strong water pumping in this compartment (blue curve, Fig 3-B). They are next entirely consumed by the microbiota in the transverse colon, consequently increasing the microbial activity, defined as the total bacterial growth rate, that reaches it maximum value in the early distal compartment. Then, the microbial metabolic activity drops off until a plateau phase that corresponds to the mucus degradation only. The microbial density (magenta curve, Fig 3-B), that is first distributed exponentially in the first part of the colon, displays a slope break in the distal part that reflects the metabolic switch from dietary fibres to mucus. The total bacterial volume fraction at the gut exit is $6 \cdot 10^{-2}$, which corresponds to a bacterial density of $0.6 \cdot 10^{11}\text{CFU}\,\text{g}^{-1}$ of feces, within the range of observed data [**?**] (see Material and Methods for unit conversions). Furthermore, the total mass of the gut microbiota is 86g and the total number of bacteria is $8.6 \cdot 10^{13}$, which correspond respectively to half and twice measured bacterial levels [**?**].

2.2.2 Spatial distribution of the microbiota and SCFA in the reference state.

The longitudinal unidimensional variations of the gut content do not account for the three-dimensional heterogeneities, and in particular the radial distributions that are observed in the microbial populations and metabolites (Fig 4). We can observe that the microbial population levels are higher in the mucosal part of the proximal and transverse compartments. This is mainly the result of the

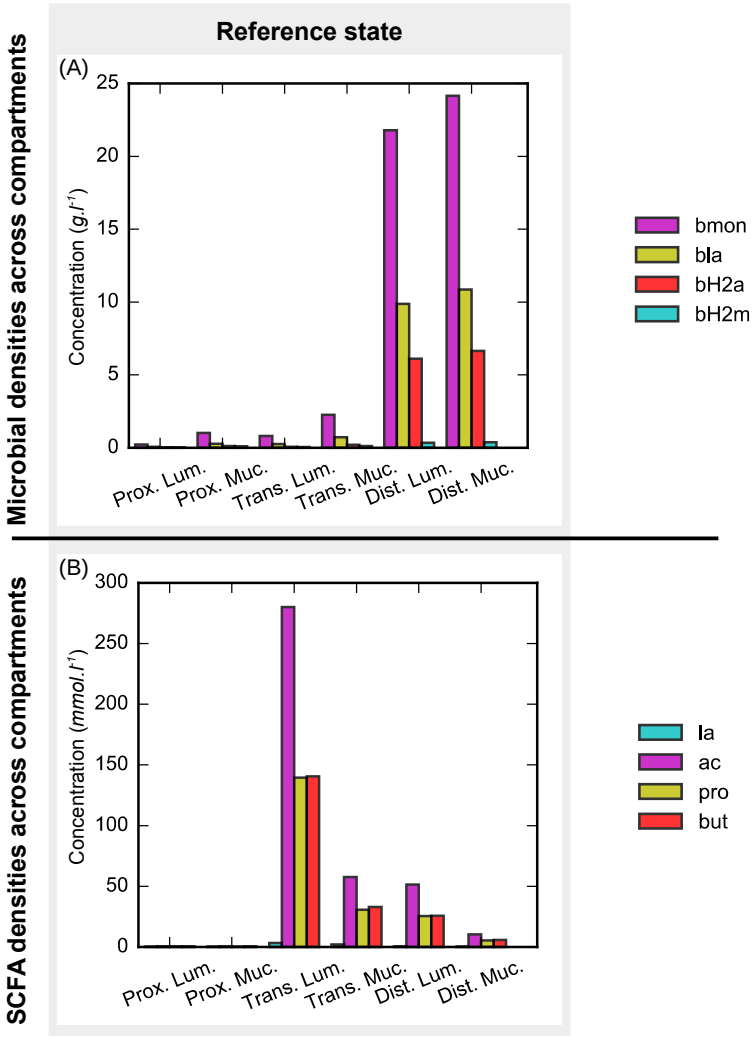

Figure 4: Microbial and SCFA levels in the different compartments. We display bar plots of the microbial population (A) and SCFA (B) averaged densities in 6 different compartments of the gut, formed by the luminal and mucosal regions in the proximal, transverse and distal colon. The mucosal area is defined by the points located at less than 0.2cm from the mucosal boundary.

important water absorption in that compartments, leading to noticeable radial speed that accumulates the mixture components near the mucosa, including the bacteria. In the distal part, where the mixture diffusion and the radial speed balance, the microbial distribution is much more homogeneous. The microbial levels reflect the trophic interactions: the top bacteria in the trophic chain, i.e. the poly/monosaccharides consumers $\mathbf{B}_{mon}$, are also the most present in each compartment. Their level reaches approximatively twice the level of the lactate consumers $\mathbf{B}_{la}$, which in turn is greater than the acetate producers $\mathbf{B}_{H_2,a}$. The

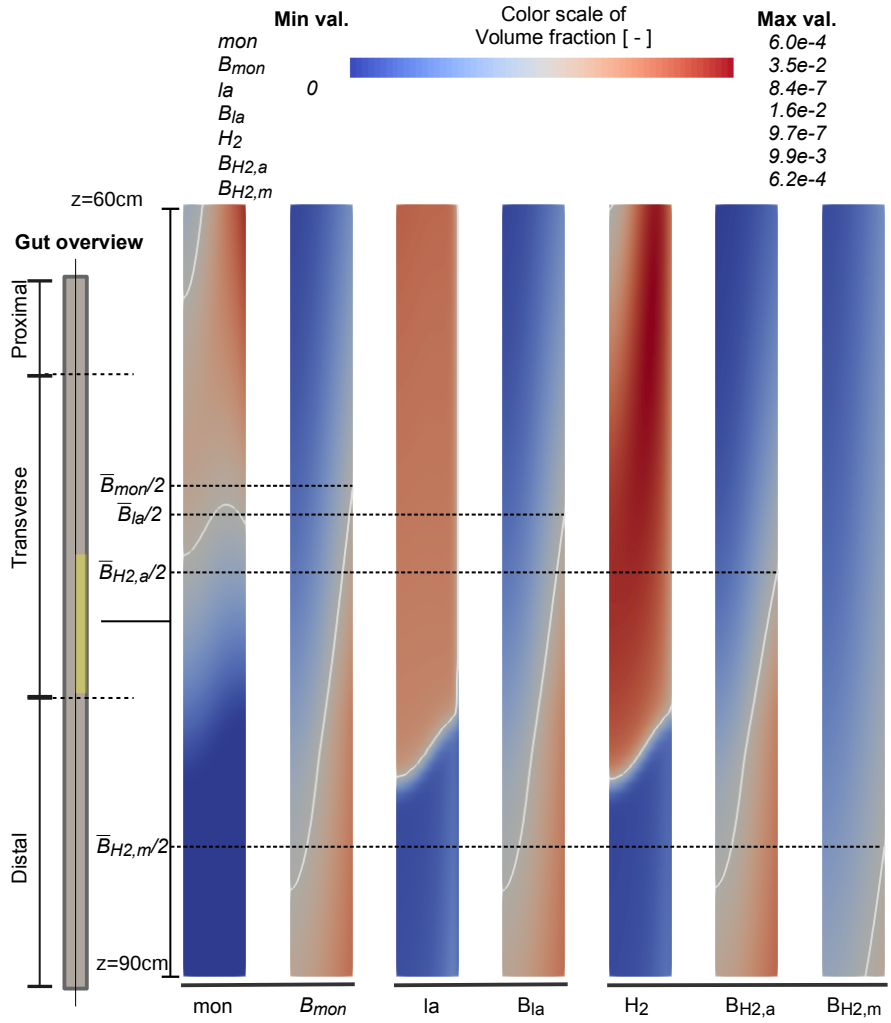

Figure 5: **Spatial distribution of the trophic chains in the transverse gut.** The steady-state distribution of each bacterial population are displayed together with their respective substrate. We represent also in each plot the isoline of half the maximal value. We indicate with dashed lines the intersection of this isovalue with the mucosa, in order to compare the longitudinal position of the bacterial fronts. We note that we represent half a plane of the cylindrical gut; the axis of the cylinder is the left boundary of the images, while the right boundary is the mucosa; the upper part of the images is the most proximal: the digestive flux is then directed from the top to the bottom of the figure.

methanogens $\mathbf{B}_{H_2,m}$, which are repressed by the increasing pH along the gut, present smaller levels. Their spatial distribution can be investigated with a better resolution (Fig. 5), but still reflects the trophic chains in the model. The population $\mathbf{B}_{mon}$, that takes in charge the upper part of the fibre metabolic pathways, is first present in the proximal part of the gut, producing lactate. Then, the $\mathbf{B}_{la}$ population breaks through and consumes rapidly the lactate, producing H_2. The density of $\mathbf{B}_{H_2,a}$ and $\mathbf{B}_{H_2,m}$ are then higher distally, after H_2 consumption. We also observe that the bacterial populations are higher in the vicinity of the mucus layer and lower in the lumen, reproducing a phenomena recently observed in vivo by fluorescence imaging with labelled microbial strains [**?**].

The SCFA concentrations are higher in the transverse lumen, where the microbial activity is high (Fig 4). In the mucosal compartment, the absorption by the host decreases the SCFA densities. In the distal part, the diffusion together with the absorption homogenizes the SCFA concentrations and decreases their overall levels. The millimolar ratio Acetate:Propionate:Butyrate in the luminal compartments are 82:41:43 in the proximal part, 74:37:37 in the transverse segment and 57:28:29 in the distal colon, in agreement with the predicted values in [**?**] and with the experimental measurements in [**?**, **?**]. The overall levels of SCFA in the transverse lumen are over-estimated by our model compared to experimental post mortem measures in this compartment (560 vs 118mM). However, in the mucosal transverse (121 predicted vs 105mM measured) and in the distal compartments (103 vs between 72.4 and 87.5mM measured), the model is in good agreement with experimental data [**?**, **?**].

2.2.3 Mucus layers :

The mucus layer structure is correctly reproduced in the reference case. In our model, the mucus is represented by the mucin density, which impacts the mixture viscosity through the mucus viscosity function μ_m (see section 3.1.3 of Material and Methods): as the sigmoidal function μ_m is very stiff, the viscosity threshold $f_{m,thr} = 0.04$ represents the limit of the mucus layer. When the mucus density is above this threshold, we will consider that the corresponding spatial point is inside the mucus layer. At steady state, the mucus layer is about 1.5mm thick in the proximal gut (Fig 6), where the microbial populations are small and the radial speed is high due to water absorption. This value is consistent with physiological data [**?**]. In the transverse colon, the inner mucus layer is thicker (4.5mm). This thickening can be explained by the diffusive process that counterbalances the radial transport in that region. The increase of the mucus layer thickness along the gut has been observed in rodents [**?**]. In the distal part, the mucus layer is consumed by the microbial populations, after the integral consumption of the fibres, and get thinner again until reaching 2.5mm.

2.3 Study of the drivers of the gut microbiota spatial structure

The reference state is perturbed by modifying a single mechanism included in the model. The consecutive steady state is compared to the reference to assess the importance of the corresponding parameter in the homoeostatic regulations.

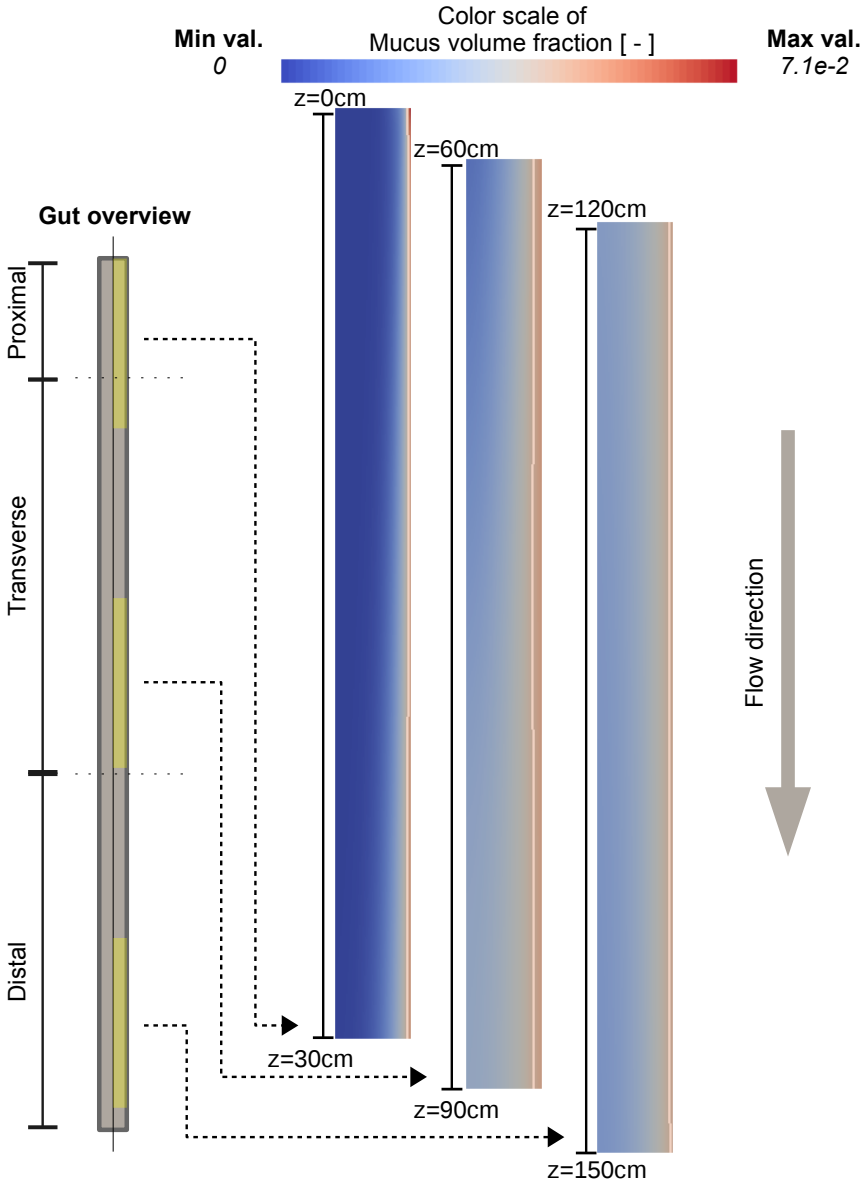

Figure 6: **Spatial distribution of the mucus in the gut.** The steady-state mucus distribution is displayed in the proximal, transverse and distal parts of the gut together with the isoline $m = 0.04$ which represents in our model the limit of the inner mucus layer: we represent half a plane of the cylindrical gut; the axis of the cylinder is the left boundary of the images, while the right boundary is the mucosa; the upper part of the images is the most proximal: the digestive flux is then directed from the top to the bottom of the figure. The mucus layer is thin in the proximal gut and get thicker in the transverse colon, to be reduced again in the distal bowel.

2.3.1 Spatial perturbations induced by diet variations.

We next assess the outcome of diet variations on the overall dynamics of our model: starting from the reference state, we impose low and high-fibre diets by respectively decreasing or increasing the averaged polysaccharide daily input by 30%, until a new steady-state is reached. We plot in Fig. 7 the speed variations induced by the diet changes, and the modification of the key parameters that were defined in Fig. 3. We observe (Fig 7, A-B) that the longitudinal speed slightly decreases or increases with the fibre intake, which is consistent with the fact that more fibres shorten the transit time in the gut. Those changes can be related to the slight discrepancies in the mucosal absorption fluxes, and consecutively in the radial speed, that can be observed in the proximal gut (Fig 7, A-B). They are sufficient to perturb the longitudinal speed. These variations in the absorption capacity are directly related in our model to the change in the level of fibres that accumulate at the mucosal boundary in the proximal gut: more fibres near the gut wall lead to less water available for absorption, and enhance the water density in the lumen and consequently, the chyme fluidity and the transit.

The differences in fibre intake impact the fibre distribution in the proximal colon (blue curves, Fig 7, C-D). The fibre concentration increases with the fibre intake, and the fibre distribution is spread out when more fibres are ingested. This phenomenon is fuelled by a higher proportion of fibres in the diet and a lower water absorption by the mucosa, reducing the material concentration in the proximal gut. This is reflected in the microbial activity distribution (red curves, Fig 7, C-D), which presents a shift of the peak activity towards the distal part for higher fibre diets. The microbial densities (magenta curves, Fig 7, C-D) in turn reflect these spatial discrepancies of microbial activity: the microbial density is first slightly higher in the transverse colon for low-fibre diet, but the tendency is rapidly reversed from the beginning of the distal bowel. The overall microbial density is higher for higher-fibre diets, as expected.

Finally, the viscosity distribution (green curves, Fig 7, C-D) also slightly varies, but in a counter-intuitive manner: if a higher viscosity could have been anticipated for the high-fibre diet, owing to the increased quantity of non-liquid mixture components (polysaccharides, bacteria) in that case, the opposite is observed. This results from two distinct phenomena. In our model, the overall mixture viscosity is driven by the mucus and the liquid densities. In the proximal and transverse bowel, the microbial levels (magenta curves, Fig 7, C-D) are higher for the low-fibre diet, enhancing the local viscosity. In the distal bowel, the bacterial levels are higher for the high-fibre diet. But, the increased microbial activity in that case (red curves, Fig 7, C-D) leads to a higher mucus degradation that counterbalances the enhancement of the bacterial levels, thus decreasing the viscosity. The mechanism is reversed for the low fibre diet in that compartment.

Differences in microbial and SCFA densities can also be observed in all the gut compartments (Fig. 8). The microbial and SCFA levels are directly linked to the quantity of dietary fibres: high-fibre diets enhance the gut function by increasing the SCFA levels, in accordance with experimental studies [**?**]. The microbial levels are first equivalent for all diets in the proximal regions, as shown in Fig. 7 C-D, but noticeable differences are observed in the distal parts.

2.3.2 Bacterial populations benefit from mucus viscosity rather than mucus degradation

Since the radial streams are important in the proximal part of the gut, we hypothesize that the bacterial populations may accumulate near the mucosa. We then study the influence of the mechanisms that drive microbes-mucus interaction included in the model: the mixture viscosity and the mucus degradation by the microbiota. We perform a simulation with a homogeneous mucus function, with a median value of $35.10^3 \mathrm{g\,cm^{-1}\,d^{-1}}$, and a simulation without mucus metabolism by the $\mathbf{B}_{mon}$ population, that we compare with the reference-fibre diet simulation (Fig. 9).

As expected, the knock out of the mucus metabolism only very slightly alters the speed fields (Fig. 9 A, where the curves are superimposed with the reference state). But the longitudinal speed is significantly reduced due to a higher water absorption in the proximal gut, when the viscosity was homogeneous (blue curve, Fig. 9 B). A reduced longitudinal speed, by enhancing the retention time, usually promotes bacterial growth. However, the bacterial activity and the overall bacterial populations are significantly reduced in the lack of viscosity heterogeneities (red and magenta curves, Fig. 9, D). These discrepancies can be explained by the local speed near the mucosa. If we compare the distribution of the longitudinal speed in the epithelium viscinity with or without viscosity heterogeneities (Fig 10, B and D), we observe a reduced velocity in the reference simulation near the mucus layer, noticeably marked in the proximal part (dashed blue lines, Fig 10, B): when the viscosity is mixture-dependant, the mucus layer enhances the local viscosity, increasing viscosity gradients, which reduces the local speed through the ratio $\Lambda(r,z)/\kappa(z)$ in the formula (19) of $u_{z,s}$. This local deceleration enhances the local retention time and promotes matter accumulation in a $7-8$mm-thick zone near the mucus layer, which reduces water availability for absorption near the gut wall. This lower water absorption in the proximal bowel leads to higher level of water in the transverse colon, which promotes bacterial growth by lowering the functional repression by volume saturation (see Table 2b for the kinetic rates of each bacterial population). When the viscosity is homogeneous, a reversed mechanism occurs, promoting water absorption, which results in a reduced bacterial growth due to volume saturation. The identification of the vicinity of the mucus layer as a slowdown zone favouring the bacterial growth is consistent with recent experiments that identified higher bacterial concentrations near the mucus layer in rodents[**?**]. We note that the reduction of the bacterial levels in the distal gut is huge when the viscosity is homogeneous (a 60% decrease comparatively to the reference), indicating that the presence of viscosity gradients is important for the bacterial colonization.

The suppression of the mucus degradation only slightly modifies the overall dynamics in the proximal part of the gut, but has a sensitive impact in the distal bowel (Fig. 9, C). In this portion of the digestive tract, there are no fibre left, and if the microbial populations are not able to metabolize the host-derived polysaccharides, the bacterial mortality is the preponderant component of the microbial activity. The overall population levels are therefore reduced in the distal part compared to the reference model. However, they are still more than 50% higher than when there is no viscosity gradient (Fig. 9, C-D).

2.3.3 Strong effect of epithelial motility and bacterial active swimming on the spatial structure.

We next investigate the effect of epithelial motility and bacterial active swimming on the overall spatial structure of the gut content. We reproduce the reference simulation with a constant peristaltic value of $U_z = -10\text{cm}\,\text{day}^{-1}$ for $5 < z < 155\text{cm}$, representing the net effect of the peristaltic and segmentation contractions of the gut wall as a upstream flow near the mucosa[**?**]. We next modify the reference simulation by endowing the microbial population with slight active swimming capabilities (with characteristic chemotactic speed of $1\text{cm}\,\text{day}^{-1}$, several orders of magnitude under the longitudinal characteristic transit speed ($100\text{cm}\,\text{day}^{-1}$) and the maximal speed observed for the bacterial swimmers, also about $100\text{cm}\,\text{day}^{-1}$ [**?**]). An asymptotic analysis of the different operators shows –see Material and Methods, section 3.2– that the active swimming in the longitudinal direction can be neglected: we then only consider the radial direction of the bacterial motility in the model. The microbial populations included in the model have therefore no possibility to swim upstream against the intestinal transit: the active motion is only possible in the radial direction, towards the lumen or the gut wall. The resultant simulations are compared to the reference experiment.

We can observe (blue curve, Fig 11,A) an important increase of the averaged longitudinal speed when the gut motility is active, which is counter-intuitive, since the peristaltic activity is applied in the upstream direction. This acceleration of the gut flow is not consecutive to a modification of the boundary conditions, which are very similar in the three cases (yellow lines, Fig. 11, A-B) except on the peaks at $z = 5\text{cm}$ and $z = 155\text{cm}$ which correspond to velocity discontinuities at the limit of application of the peristaltic activity. The higher averaged speed when the gut motility is applied comes from a redistribution of the longitudinal speed along the gut radius (Fig. 12). Upstream speeds are observed near the gut wall in the peristaltic case (Fig. 12,A), versus null speeds for the reference and the chemotactic experiments (Fig. 12,B), resulting in a large increase of the longitudinal speed in the luminal part to preserve the volume (Fig. 12,A). Namely, if some material is transported upstream in the wall viscinity, as no outflux is possible in the proximal gut, a higher speed must be applied in the lumen to evacuate this additional material income in order to prevent volume expansion in the proximal gut. The difference of order of magnitudes between the small upstream speed near the mucosa and the large downstream speed at $r = 0$ is due to the cylindrical geometry. In cylindrical coordinates, the elementary volumes near the wall are larger than the luminal ones. Hence, for a same transport speed, the amount of fluid transported in the epithelial vicinity is higher than in the lumen. Consequently, a higher speed must be applied near the gut axis than close to the mucosa in order to insure volume conservation. Regarding the speeds components, the chemotactic activity of the bacterial has a very little impact (Fig 11,B and Fig. 12,B-D).

As expected, the gut motility induces a shift towards the ileocaecal valve of the microbial populations, enhancing the bacterial functional activity in the upper transverse colon and promoting a fast consumption of the fibres in the proximal gut (magenta, red and blue curve, Fig 11,C). The bacterial active swimming also promotes an earlier colonization of the gut, shifting the microbial levels towards $z = 0$, but with smaller magnitude (magenta red and blue

curves, Fig 11,D). However, the bacterial metabolism is noticeably boosted in that case, speeding up the carbohydrate consumption, comparatively to the reference simulation (red curve, Fig 11,D). The viscosity (green curves, Fig 11,C-D) is noticeably impacted by the gut motility, which may be related to local modifications on the mucus distribution, but not by the bacterial active motion. We can observe than the gut motility has a focal impact on the overall microbial populations, with a massive increase in the proximal gut and a lower increase at the end of the distal gut, whereas the enhancement of the bacterial levels are more regular along the gut after activation of the chemotactic capabilities (magenda curves, Fig 11,C-D). We emphasize that very low motile capabilities toward the mucosa, with no longitudinal upstream swimming included in the model, are sufficient to get this positive impact on the total microbial densities.

2.3.4 Deciphering the multifactorial process of spatial structure with sensitivity analysis

We now check that the previous mechanisms result in a positive outcome when combined, i.e., that their respective effects do not compensate each other resulting in a null net effect on the gut content composition. We can observe (blue line, Fig. 13) that the polysaccharide density drops down verly early in the colon, while the bacterial activity reaches its maximal value at the end of the proximal gut. This maximal value is lower in magnitude compared to the reference experiment, but the functional activity of the microbial population is noticeably more intense in the majority of the gut length. The bacterial populations start growing at the beginning of the proximal gut, which is a strong improvement comparatively to the reference experiment where the microbial colonization was effective at the early distal gut only. At the end of the distal bowel, the overall bacterial levels are increased up to 30% compared to the reference. The viscosity repartition is less impacted by the combination of the different mechanisms: a relatively weak decrease in the average is observed, probably related to a higher mucus consumption.

A more accurate study is performed through a global sensitivity analysis of the different parameters. We shift conjointly the parameters defining the mixture viscosity, the gut motility intensity, the bacterial swimming magnitude and the fibre input to assess their impact on the overall bacterial repartition along the gut. Namely, we study for each $z \in (0, L)$ the variations of the radially averaged total bacterial population $B(z) := \sum_{i \in I_B} \frac{2}{R^2} \int_0^R r c_i(z, r) dr$ when varying the parameters, where I_B is the set of bacterial populations and c_i, $i \in I_B$ the different microbial levels (see the Material and Methods for a precise description of the sensitivity analysis methodology and the notations). We can check in the upper panel of Fig. 14 that the outputs are quite dispersed around the median: large differences are observed between extremal values (dashed red lines), and the second and third quartiles (grey zone) are quite spread out, in a range of about 20 % of the median value in the middle of the gut. The magnitude of the dispersion is relatively stable along the gut, with a small increase in its proximal and very distal parts. The lower panel displays the Sobol index $S_\theta(z)$ of the different parameters θ that were tested, for $z \in (0, L)$, i.e. the contribution of a given parameter to the total variance of the model outputs. The precise definition is given in section 3.5 in Material and Methods. We can observe that the gut motility is the main driver of the spatial structure of the bacterial pop-

ulations in the proximal gut while the level of fibre input is preponderant in its transverse and distal parts. The peak of active swimming impact is located at the beginning of the transverse colon, but its influence is small compared to gut motility and fibre levels. The effect of viscosity variation is very small all along the gut, with a peak in the very proximal track. This indicates that, despite the necessity of viscosity gradients to obtain physiological bacterial levels (see subsection 2.3.2 above), the discrepancies between higher and smaller viscosity values are not determinant for the microbial growth: the preponderant mechanism could therefore be related to threshold effects in the sharp distribution of the viscosity values near the mucusa, rather than the effective values of viscosity in the lumen and in the mucus layer.

3 Material and methods

3.1 Mathematical model of the gut microbiota and its metabolic substrate

We present the mathematical framework, emphasizing the underlying biological assumptions of the model and the modelling of the different mechanisms able to impact the spatial structure of the microbiota.

3.1.1 Geometrical assumptions

The fluid and population dynamics PDEs are set on a cylindrical domain $\Omega = \omega \times [0, L]$ of $\mathbb{R}^3$ that represents the geometry of the colon, $L = 154$cm being its length and $\omega \subset \mathbb{R}^2$ its transverse section, which is a disc of radius $R = 2.5$cm. We note by $\Gamma_{in} := \omega \times \{0\}$, $\Gamma_{out} := \omega \times \{L\}$ and $\Gamma_m = \partial\Omega \setminus (\Gamma_{in} \cup \Gamma_{out})$ respectively the proximal extremity (just after the ileocaecal valve), the distal boundary (which is set in the middle of the sigmoid colon, before the rectum) and the mucosal wall of the colon. Physiological compartments can be identified as portions of the total cylinder: the proximal, transverse and distal colons have a respective length of $L_{prox} = 21$cm, $L_{trans} = 50$cm and $L_{dist} = 83$cm [**?**]. The total length is shorter than the averaged physiological colorectal length, which is about 190cm [**?**, **?**], because we do not consider the end of the sigmoid and the rectal parts.

3.1.2 Global structure of the model.

We consider a mixture model [**?**, **?**, **?**] of the multiphasic intestinal content. Among the different entities considered in this model, we discriminate between the mixture components that are large enough to produce mechanical forces, hence impacting the fluid mechanics, and the diffusing compounds dissolved in the intestinal mixture, without any impact on the mixture flow. To determine the different metabolic elements to be included in the model, we follow the strategy introduced in [**?**]: we assume that the fibres, which are the predominant source of raw material for metabolic activity, are determinant for the spatial organization of the microbiota and we consider the different metabolites involved in the fibre degradation model in the gut introduced in [**?**].

This model is composed of four functional microbial metapopulations, each involved in different stages of polysaccharides metabolic pathways. The first

population, called $\mathbf{B}_{mon}$, hydrolyses the fibres and mucus polysaccharides to produce monosaccharides, that are metabolized in turn to support their growth, producing lactate, SCFA (acetate, propionate and butirate) and dissolved gas (H_2 and CO_2). The population $\mathbf{B}_{la}$ then grows on lactate and produces SCFA and gas, while the populations $\mathbf{B}_{H_2a}$ and $\mathbf{B}_{H_2m}$ are fuelled by the di-hydrogen, through respectively the homeoacetogenesis and methanogenesis pathways. In order to maintain physiological gas concentration in the liquid, we model vaporisation to gaseous phase. We finally get 13 processes (see Fig. 2 for a synoptic view of the reactions involved in the model). The different bacterial populations are gathered in the set $I_B = \{\mathbf{B}_{mon}, \mathbf{B}_{la}, \mathbf{B}_{H_2a}, \mathbf{B}_{H_2m}\}$. We assume that, among those entities, the larger elements susceptible to influence the fluid mechanics are the mucus (m), the polysaccharides (pol), the 4 bacteria (I_B), the liquid chyme (l) and indigestible residuals (r) that are not metabolized by bacteria but do impact the local rheology. We thus collect those mixture components in the 8 elements set $I_C = \{m, pol, \mathbf{B}_{mon}, \mathbf{B}_{la}, \mathbf{B}_{H_2a}, \mathbf{B}_{H_2m}, l, r\}$. The dissolved compounds (which include, among other, the gas and SCFA involved in the model) are collected in the set $I_S = \{mon, lac, H_2, ac, pro, bu, CH_4, CO_2\}$ for respectively the monosaccharides, the lactate, the hydrogen, the acetate, the propionate, the butyrate, the methane and the carbone dioxyde. We note that, unlike [**?**], we do not explicitly introduce a gaseous phase in the model.

In the following, we will describe in details the equations that govern the evolution of mass fractions of the mixture components and the evolution of concentrations of dissolved compounds, by using mass balance equations. These equations contain some source terms coming from the metabolic reactions, which involve some transfers of mass from one phase to another. They also include some transport terms, for which we need to compute the velocity of the mixture thanks to fluid dynamics considerations.

3.1.3 Mass conservation equations

As all the phases of the multiphasic gut content are mainly composed of water, we assume that they all have the same constant density $\rho_{f_i} = 1\,\mathrm{g\,cm^{-1}}$. For simplification purposes, we also take the same diffusion coefficient for all phases. The mixture state is then totally described by the volume fraction f_i of its phases.

We model the time evolution of the volume fraction of the component $i \in I_C$ by the following reaction-diffusion-convection equation:

$$\partial_t f_i - \mathrm{div}(\sigma \nabla f_i) + \mathrm{div}(u_i f_i) = F_i, \tag{1}$$

where σ ($\mathrm{cm^2\,day^{-1}}$), u_i ($\mathrm{cm\,day^{-1}}$) and F_i ($\mathrm{day^{-1}}$) respectively represent the diffusion coefficient, the transport speed and the metabolic transformation rate of the mixture component i. The definition of the source term F_i will be detailed later on. Nevertheless, for the modelling issues, it is important to bear in mind that the phase-to-phase transfers embodied into the F_i's are volume invariant which amounts to assume that :

$$\sum_{i \in I_C} F_i = 0. \tag{2}$$

For the derivation of the equations, we are also going to use the fact that the mixture fills up the whole intestinal volume resulting in the following saturation

constraint

$$\sum_{i \in I_C} f_i(t,x) = 1, \quad \forall x \in \Omega, \quad \forall t > 0. \tag{3}$$

The mass conservation equations of the dissolved metabolites are derived following [**?**]. We assume that the dissolved compounds concentrations and their diffusion coefficients are locally the same in every mixture phase. We also assume that all the dissolved compounds are convected with the same velocity and we set the compound transport velocity as the local weighted average $\tilde{u} = \sum_{i \in I_C} u_i f_i$ ($\mathrm{cm\,day^{-1}}$) of the mixture phases speeds. We finally get the following mass conservation reaction-diffusion-convection equation for the concentration of the chemical j

$$\partial_t c_j - \mathrm{div}(\sigma_j \nabla c_j) + \mathrm{div}(c_j \tilde{u}) = G_j \tag{4}$$

where σ_j ($\mathrm{cm^2\,day^{-1}}$) and G_j ($\mathrm{mol\,cm^{-1}\,day^{-1}}$) are the diffusion coefficient of the diffusing compound j and its reaction rate. The definition of the source term G_j will also be precisely defined later on.

3.1.4 Units of the model

The time and space values are expressed in day and cm. The mixture components are dimensionless, since they represent volume fractions. However, as we assumed that all the phases have the water density $\rho_{f_i} = 1\mathrm{g\,cm^{-1}}$, the volume fractions can be easily converted to massic densities. To allow comparisons with the usual units of bacterial levels in microbiology literature, such as Colony Forming Units per grammes ($\mathrm{CFU\,g^{-1}}$) which is linked to the number of living microbes per mass unit, we assumed that the average volume of a single bacteria is $1\mu\mathrm{m}^3 = 10^{-12}\mathrm{cm}^3$. Thus, a direct conversion between bacterial volume fractions and $\mathrm{CFU\,g^{-1}}$ of gut content can be obtained by applying a multiplicative factor of 10^{12} to the bacterial volume fraction. The densities of the dissolved compounds are expressed in $\mathrm{mol\,cm^{-3}}$. The units of the different model parameters are detailed in the Tables 1, 3 and 4.

We now detail the biological assumptions behind every processes.

3.1.5 Diffusion and Transport speeds

When the mixture is at rest, i.e. when the different transport terms are null, the phases are supposed to inter-penetrate each other by diffusion: we assume that the interface forces are not sufficient to maintain a sharp separation of the different phases. As this diffusive process is supposed to be small comparatively to the transport process, we model that feature with the diffusive term $\mathrm{div}(\sigma \nabla f_i)$, modelled with a simple Fick's law, where σ is a uniform diffusion coefficient that does not depend on the mixture phase.

Each fluid component f_i is supposed to be transported with the same mixture speed u derived from the fluid mechanics, which can be corrected, for the bacteria only, by an active motion towards a metabolite source modelled by a chemotactic advection term $\vartheta_{i,chem}$ [**?**, **?**], giving an apparent speed field

$$u_i = u + \vartheta_{i,chem}. \tag{5}$$

Using (3), this gives the following velocity for the dissolved compounds mass equation :

$$\tilde{u} = u + \sum_{i \in I_C} \vartheta_{i,chem} f_i$$

3.1.6 Microbial active motion

For each bacteria $i \in I_B$, the active motion is modelled by the Keller-Segel model: the gradient of a chemotactic potential influences the resulting velocity, which is therefore defined as $\vartheta_{i,chem} = \sum_j \lambda_{ij} \nabla \Phi_j$, where Φ_j is the chemotactic potential created by the metabolite j and $\lambda_{i,j}$ is the chemosensitivity coefficient for the bacteria i and the metabolite j [**?**, **?**]. The chemotactic potential of the metabolite $k \in I_S \cup \{m, pol\}$ is defined up to a constant through the resolution of the Poisson equation, when $k \in I_S$,

$$\begin{aligned} -\Delta \Phi_k = c_k - \frac{1}{|\omega|} \int_\omega c_k(x,z)dx \quad & \text{in } \Omega \\ \nabla \Phi_k \cdot \eta = 0 \quad & \text{on } \partial\Omega. \end{aligned} \tag{6}$$

or, when $k \in \{m, pol\}$,

$$\begin{aligned} -\Delta \Phi_k = f_k - \frac{1}{|\omega|} \int_\omega f_k(x,z)dx \quad & \text{in } \Omega \\ \nabla \Phi_k \cdot \eta = 0 \quad & \text{on } \partial\Omega. \end{aligned} \tag{7}$$

The term $\frac{1}{|\omega|} \int_\omega c_k(x,z)dx$ (resp.$\frac{1}{|\omega|} \int_\omega f_k(x,z)dx$) is a compatibility condition for Eq. (6) (resp. (7)) to be solvable, which is different from the usual one. Indeed, usually, this term is averaged on the whole domain, that is to say $\frac{1}{|\Omega|} \int_\Omega c_k(x,z)dxdz$ (resp. $\frac{1}{|\Omega|} \int_\Omega f_k(x,z)dxdz$). In the following of the paper, a simplification model will be proposed when the aspect ratio of the gut goes to 0, see Sec. 3.2. In the asymptotic limit, the longitudinal chemotactic forces vanish, and the operator $\Delta \Phi_k$ degenerates in $\frac{1}{r}\partial_r(r\partial_r \Phi_k)$: the chemotactic active swimming thus occurs in the radial direction only. The term $\frac{1}{|\omega|} \int_\omega c_k(x,z)dx$ (resp.$\frac{1}{|\omega|} \int_\omega f_k(x,z)dx$) enables to provide also a compatibility condition in the case of the asymptotic limit of Eq. (6) (resp. (7)). We refer to [**?**] for details.

3.1.7 Fluid dynamics model:

Adding Eq. (1) for every $i \in I_C$, together with Eq. (2) and Eq. (5), we get a constraint on the speed fields

$$\operatorname{div}(\sum_{i \in I_C} f_i u_i) = \operatorname{div}(\tilde{u}) = 0, \quad \text{i.e.,} \quad \operatorname{div}(u) = -\operatorname{div}(\sum_{i \in I_B} f_i \vartheta_{i,chem}). \tag{8}$$

This contraint enables us to write Eq.(4) as follows :

$$\partial_t c_j - \operatorname{div}(\sigma_j \nabla c_j) + \tilde{u} \cdot \nabla c_j = G_j \tag{9}$$

This constraint is supplemented by a momentum conservation equation: we model the mixture speed with the following Stokes equation on u

$$\nabla p - \mathrm{div}(\mu D(u)) = 0 \tag{10}$$

where $D(u) = \frac{1}{2}(\nabla u + \nabla u^t)$ and p is a pressure, that is to say a Lagrange multiplier which ensures the effectivity of the constraint (8). In this expression, μ ($\mathrm{g\,cm^{-1}\,day^{-1}}$) is the apparent mixture viscosity, which depends on space and time through volume fractions, as defined in the following paragraph.

3.1.8 Definition of the viscosity:

We assume that the local viscosity is inhomogeneous and depends on the local mixture composition, resulting in an explicit coupling between the fluid components and the speed field. We consider that the main drivers of the local mixture viscosity are the mucus and the liquid chyme volume fractions. We set

$$\mu(x,z,t) = \max(\mu_m(f_m(x,z,t)), \mu_l(f_l(x,z,t)))$$

where μ_m (resp. μ_l) stands for a function describing the mucus rheology (resp. the luminal rheology) and depending on the mucus fraction volume (resp. the liquid volume fraction).

Following [**?**], we first sketch the highly viscous gel-like mucus layer by defining μ_m as a sigmoid function. A threshold level of mucine $f_{m,thr}$ is defined as a marker of the mucus layer: above this threshold, we consider that the mixture is actually mucus and it is assigned a value close to the mucus viscosity $\mu_{max,m}$. Under this level, the contribution of μ_m to the overall viscosity is close to a small value $\mu_{min,m}$. The transition between both values is tuned by a parameter λ_m. We namely set

$$\mu_m(f_m) = \mu_{min,m} + (\mu_{max,m} - \mu_{min,m})\frac{f_m^{2\lambda_m}}{f_{m,thr}^{2\lambda_m} + f_m^{2\lambda_m}}$$

The luminal rheology is defined in the same way based on the liquid phase l: the more liquid l, the less viscous is the mixture, which leads to

$$\mu_l(f_l) = \mu_{max,l} - (\mu_{max,l} - \mu_{min,l})\frac{f_l^{2\lambda_l}}{f_{l,thr}^{2\lambda_l} + f_l^{2\lambda_l}}.$$

We chose the parameters of the sigmoidal functions so that the sharp transition between the minimal and maximal values of the viscosity occurs in $(0,1)$, where the volume densities f_m and f_l lie.

3.1.9 Metabolic activity

We note P_c and P_s the reaction matrices for the mixture components and the solutes that define the yield of each process on the corresponding compounds, based on stoichiometry [**?**] (see Table 2, where Y_{j,P_i} denotes the stoichiometric coefficient related to component $j \in I_C \cup I_S$ in process P_i).

We also introduce K the kinetic rate vector, which components are defined by $k_p\rho_p$ for the different processes p under consideration. For each process, k_p represents a unitary maximal kinetic rate whereas ρ_p models saturation effects. Namely, ρ_p is a Monod-like function for each metabolic process, except for the fibre and mucus hydrolysis, that is modeled with a Comtois law, following [**?**] (

Geometrical parameters				
Parameter	Value	Unit	Description	Ref.
L	154	cm	total gut length	[?]
R	2.5	cm	gut radius	[?]
L_{prox}	21	cm	Proximal colon length	[?]
L_{trans}	70	cm	Transverse colon length	[?]
L_{dist}	63	cm	Distal colon length	[?]
Diffusion parameters				
Parameter	Value	Unit	Description	Ref.
σ	0.8	$cm^2\,d^{-1}$	Diffusion coeff.: mixture comp.	-
σ_{mon}	1.4	$cm^2\,d^{-1}$	Diffusion coeff.: mono.	-
σ_{la}	1.4	$cm^2\,d^{-1}$	Diffusion coeff.: lactate	-
σ_{ac}	1.4	$cm^2\,d^{-1}$	Diffusion coeff.: acetate	-
σ_{pro}	1.4	$cm^2\,d^{-1}$	Diffusion coeff.: proprionate	-
σ_{but}	1.4	$cm^2\,d^{-1}$	Diffusion coeff.: butyrate	-
σ_{H_2}	0.8	$cm^2\,d^{-1}$	Diffusion coeff.: H_2	-
σ_{CH_4}	2	$cm^2\,d^{-1}$	Diffusion coeff.: CH_4	-
σ_{CO_2}	2	$cm^2\,d^{-1}$	Diffusion coeff.: $C0_2$	-
Viscosity parameters				
Parameter	Value	Unit	Description	Ref.
$\mu_{min,l}$	$0.864 \cdot 10^3$	$g\,cm^{-1}\,d^{-1}$	Water viscosity	[?]
$\mu_{max,l}$	$36.7 \cdot 10^3$	$g\,cm^{-1}\,d^{-1}$	Visc. of dried mixture.	-
$f_{l,thr}$	0.5	[−]	Viscosity threshold: liquid sigmoid	-
λ_l	2	[−]	Stiffness: liquid sigmoid	-
$\mu_{min,m}$	$0.864 \cdot 10^3$	$g\,cm^{-1}\,d^{-1}$	Water viscosity	[?]
$\mu_{max,m}$	$73.4 \cdot 10^3$	$g\,cm^{-1}\,d^{-1}$	Mucus viscosity	[?]
$f_{m,thr}$	0.0425	[−]	Viscosity threshold: mucus sigmoid	-
λ_m	7	[−]	Stiffness: mucus sigmoid	-
Initial condition				
Parameter	Value	Unit	Description	Ref.
$f_{min_{init},m}$	0	[−]	No mucus in lumen	[?]
$f_{max_{init},m}$	0.05	[−]	Max. quantity of mucins	[?]
r_m	2.25	cm	Threshold: initial condition	-
$\lambda_{m,init}$	4	[−]	Stiffness: initial condition	-

Table 1: **Geometrical, diffusion, viscosity and initial condition parameters.** The diffusion coefficients are calculated from order of magnitude of reported diffusion coefficients of the different compounds in water [?] multiplied by the corresponding diffusive ratio between water and mucus as reported in [?]. The viscosity of the dried mixture was set to half the mucus viscosity.

see Table 2). Finally, if $F = (F_i)_{i\in I_C}$ and $G = (G_j)_{j\in I_S}$, we have the following relations :

$$F = P_c K \text{ and } G = P_s K. \tag{11}$$

To ensure the volume-conservation condition (2), we consider that mucus or polysaccharides consumption, or bacterial death, releases an equivalent volume of water in the liquid chyme (see volume transfers in Fig. 2). Conversely, an equivalent volume of water is removed during bacterial growth: in order to satisfy the constraint (3), we then modulate the bacterial growth with the local volume fraction, which stands for modelling that bacterial populations must be in contact with liquid to be able to grow (see Table 2b for the kinetic rates of each population). Following [?], an additional pH-dependant-repression is introduced for the metanogens $b_{H_2,m}$ through the introduction of a space dependant linear pH function $pH(z) := I_{pH_{min}} + (I_{pH_{max}} - I_{pH_{min}})z/L$ and a

multiplicative factor $I_{pH}(z)$ applied to ρ, where

$$I_{pH}(z) := exp\left(-3(\frac{pH(z) - I_{pH_{High}}}{I_{pH_{High}} - I_{pH_{Low}}})^2\right) \mathbb{1}_{Ph(z)<I_{pH_{High}}} + \mathbb{1}_{Ph(z)\geq I_{pH_{High}}}$$

The bacteria are assigned a constant death rate. We finally note that, as the gaseous phase is not modelled, we do not introduce any equilibrium between dissolved components and gas in gaseous phase. However, we prevent accumulation of dissolved gas in the solution by adding for $j \in \{CH_4, CO_2, H_2\}$ and for the corresponding process P_i, a term in the source term G_j defined as (see also Table 2b) $k_i \left(c_j - K_{h,P_i} RT[c_{j_g}]_\infty\right)$, where $[c_{j_g}]_\infty$ is the asymptotic value of the corresponding gas in the proximal luminal part of [**?**], and R and T are the perfect gas constant and the temperature. It is equivalent to define a Henry law with a stationary homogeneous gas phase.

We gather in Table 2 the precise definition of the reaction matrices and the growth rates. The values for all the parameters Y_{g,P_i}, k_p, K_{h,P_i}, K_{x,P_i}, K_{s,P_i}, $[j_g]_\infty$, R and T are given in Table 3.

3.1.10 Mass transfers through the boundaries.

The modelling of the mass transfers through the boundaries is a key step since they account for the lumen-epithelium exchanges, which are central both in the fluid dynamics and in the metabolic activity through metabolite absorption and release.

The chemotactic speed being null at the boundaries, we supplement the mass conservation equations (1) and (9) by the natural Robin boundary conditions:

$$(-\sigma \nabla f_i + u f_i) \cdot \eta = \gamma_{f_i} \quad \text{and} \quad (-\sigma_j \nabla c_j + \tilde{u} c_j) \cdot \eta = \gamma_{c_j} \quad \text{on } \Gamma, \qquad (12)$$

where η is the unitary outgoing normal vector to the boundary. It remains to detail the boundary fluxes γ_{f_i} and γ_{c_j}, that model the mass transfers through the boundaries. According to the cases, γ_{f_i} and γ_{c_j} are either some constant values, either functions of the space variables, either functions of the phases volume fractions.

Dietary inflow: we define a speed profile $u_{in} = u \cdot \eta$ on Γ_{in} such that its average is equal to $< u_{in} >= V_{in}/|\omega|$ where V_{in} is the daily volume of digestat that reaches the colon. The dietary inflow of fibres, bacteria and monosaccharides is then defined with the formula $\gamma_{f_i} =< u_{in} > f_{i,in}$ on Γ_{in} where $f_{i,in}$ is the component density in the inflow. Similarly, we will set $\gamma_{c_j} =< u_{in} > c_{j,in}$ on Γ_{in}. Values $< u_{in} >$, $f_{i,in}$ and $c_{j,in}$ are given in agreement with biological observations, see Table 4.

Water pumping through the mucosa: following [**?**], we define the strongest water pumping rate $\gamma_{l,max}$ in the proximal part of the gut mucosa, followed by a linear diminution of the water uptake, and finally a smaller basal activity $\gamma_{l,min}$ on the distal part. Let us denote by $(0, Z_p)$ (resp. (Z_d, L)) the longitudinal coordinates for the proximal part (resp. the distal part), we define, on Γ_m

$$\gamma_{f_l} = \gamma_{l,max} f_l \text{ for } z = (0, Z_p), \quad \gamma_{f_l} = \gamma_{l,min} f_l \text{ for } z = (Z_d, L),$$

$$\gamma_{f_l} = \left(\gamma_{l,max} - \frac{z - Z_p}{Z_d - Z_p}(\gamma_{l,max} - \gamma_{l,min})\right) f_l \text{ for } z = (Z_p, Z_d).$$

	P1	P2	P3	P4	P5	P6	...
l	1	1	$-Y_{\mathbf{B}_{mon},P3}$	$-Y_{\mathbf{B}_{la},P4}$	$-Y_{\mathbf{B}_{H_2a},P5}$	$-Y_{\mathbf{B}_{H_2m},P6}$	...
m	-1						...
pol		-1					...
$\mathbf{B}_{mon}$			$Y_{\mathbf{B}_{mon},P3}$				...
$\mathbf{B}_{la}$				$Y_{\mathbf{B}_{la},P4}$			...
$\mathbf{B}_{H_2a}$					$Y_{\mathbf{B}_{H_2a},P5}$		...
$\mathbf{B}_{H_2m}$						$Y_{\mathbf{B}_{H_2m},P6}$	...
r							...
mon	$Y_{mon,P1}$	$Y_{mon,P2}$	-1				...
la			$Y_{la,P3}$	-1			...
ac			$Y_{ac,P3}$	$Y_{ac,P4}$	$Y_{ac,P5}$		...
pro			$Y_{pro,P3}$	$Y_{pro,P4}$			...
but			$Y_{but,P3}$	$Y_{but,P4}$			...
CH_4						$Y_{CH_4,P6}$	...
CO_2			$Y_{CO_2,P3}$	$Y_{CO_2,P4}$	$Y_{CO_2,P5}$	$Y_{CO_2,P6}$	...
H_2			$Y_{H_2,P3}$	$Y_{H_2,P4}$	-1	-1	...

...	P7	P8	P9	P10	P11	P12	P13	
...	1	1	1	1				l
...								m
...								pol
...	-1							$\mathbf{B}_{mon}$
...		-1						$\mathbf{B}_{la}$
...			-1					$\mathbf{B}_{H_2,a}$
...				-1				$\mathbf{B}_{H_2,m}$
...								r
...								mon
...								la
...								ac
...								pro
...								but
...					-1			CH_4
...						-1		CO_2
...							-1	H_2

(a) Reaction matrix P_c (white background) and P_s (grey background).

	P1	P2	P3	P4	P5
ρ	$\frac{f_m \cdot f_{\mathbf{B}_{mon}}}{K_{x,P1} f_{\mathbf{B}_{mon}} + f_m}$	$\frac{f_{pol} \cdot f_{\mathbf{B}_{mon}}}{K_{x,P2} f_{\mathbf{B}_{mon}} + f_{pol}}$	$f_l \frac{c_{mon} \cdot f_{\mathbf{B}_{mon}}}{K_{s,P3} + c_{mon}}$	$f_l \frac{c_{la} \cdot f_{\mathbf{B}_{la}}}{K_{s,P4} + c_{la}}$	$f_l \frac{c_{H_2} \cdot f_{\mathbf{B}_{H_2a}}}{K_{s,P5} + c_{H_2}}$
k	k_{P1}	k_{P2}	k_{P3}	k_{P4}	k_{P5}

	P6	P7	P8	P9	P10
ρ	$f_l \frac{c_{H_2} \cdot f_{\mathbf{B}_{H_2m}}}{K_{s,P6} + c_{H_2}} I_{pH}$	$f_{\mathbf{B}_{mon}}$	$f_{\mathbf{B}_{la}}$	$f_{\mathbf{B}_{H_2a}}$	$f_{\mathbf{B}_{H_2m}}$
k	k_{P6}	k_{P7}	k_{P8}	k_{P9}	k_{P10}

	P11	P12	P13
ρ	$c_{CH_4} - K_{h,P11} RT [CH_{4,g}] \infty$	$c_{CO_2} - K_{h,P12} RT [CO_{2,g}] \infty$	$c_{H_2} - K_{h,P13} RT [H_{2,g}] \infty$
k	k_{P11}	k_{P12}	k_{P13}

(b) Vector of the kinetic rates.

Table 2: Petersen matrices and kinetic rate vectors.

Mucus production: we consider that the mucosa insures the mucus layer homeostasis by a regulatory mechanism that produces mucus when the mucus level is below a threshold $f_{m,tr}$ and consumes mucus otherwise. We then set on Γ_m

$$\gamma_{f_m} = \gamma_m(f_m - f_{m,tr})$$

where γ_m is the mucus production rate.

On Γ_m, we also set $\gamma_{f_i} = 0$ when $i \in I_C \setminus \{l, m\}$

SCFA and other compounds absorption: we set on Γ_m a linear distribution of SCFA absorption along the mucosal wall between a maximal absorption rate $\gamma_{j,max}$ in the proximal part and a minimal rate $\gamma_{j,min}$ in the distal part, for the SCFA j. We then set

$$\gamma_{c_j} = \gamma_{j,max} - (\gamma_{j,max} - \gamma_{j,min})z/L \text{ for } j \in \{la, ac, pro, bu\}$$

and

$$\gamma_{c_j} = 0 \text{ otherwise.}$$

Outflow: summing the mass conservation equations (1) for all $i \in I_C$ together with the saturation constraint (3), the volume conservation constraint (2) and the boundary conditions (12), and integrating on Ω shows that

$$\int_{\Gamma_{out}} u.\eta = \sum_{i \in I_C} \int_{\Gamma_{in} \cup \Gamma_m} \gamma_{f_i}.$$

In other words, the outflow balances the other mass transfers through the boundaries to conserve the overall volume.

We then set on Γ_{out}, for all $i \in I_C$, $\gamma_{f_i} = u_i \cdot \eta f_i$ and for all $j \in I_S$, $\gamma_{c_j} = \tilde{u} \cdot \eta c_j$.

3.1.11 Epithelial motility and peristaltism:

To close the overall system, it only remains to define boundary conditions for the speed through Γ_m. We set η as the local unitary outgoing normal vector, η_z the longitudinal tangential unitary vector (i.e. $\eta_z = (0, 0, 1)$ on Γ_m and $\eta_z = (1, 0, 0)$ on Γ_{out} in cylindrical coordinates), and $\eta_r = \eta_z \wedge \eta$ the radial tangential unitary vector, we take

$$u_i \cdot \eta = \sum_{i \in I_C} \gamma_{f_i} + U_{per,r}, \quad u_i \cdot \eta_z = U_{per,z}, \quad u_i \cdot \eta_r = 0 \text{ on } \Gamma_m, \tag{13}$$

where $U_{per} = (U_{per,r}, 0, U_{per,z})$ is a speed describing the net motile activity of the mucosal wall, including peristaltism and segmentation contractions. Those values are set to 0 in the reference state.

3.2 Model simplification

For the sake of completness, we outline the simplification method that is detailled in [**?**]. Using cylindrical coordinates (r, θ, z), we assume first that the state of our system is independent of θ. Exploiting the aspect ratio of the gut, where $\varepsilon := L/R \ll 1$, we search for solutions of equations (1)-(13) under the form

$$f_i = f_i^{(0)} + \varepsilon f_i^{(1)} + \varepsilon^2 f_i^{(2)} + \cdots, \quad c_j = c_j^{(0)} + \varepsilon c_j^{(1)} + \varepsilon^2 c_j^{(2)} + \cdots, \quad u = u^{(0)} + \varepsilon u^{(1)} + \varepsilon^2 u^{(2)} + \cdots.$$

The first order asymptotic approximation of the solution solves the following equations [**?**], where $\mathrm{div_r}$ is the divergence operator in cylindrical coordinates (i.e. $\mathrm{div_r}\, u := \frac{1}{r}\partial_r(ru_r) + \partial_z(u_z)$ where $u = (u_r, u_z)$ is a vector in cylindrical coordinates) and ∇_r is the gradient operator in cylindrical coordinates i.e. $\nabla_\mathrm{r}\, c = (\partial_r c, \partial_z c)$. Therefore, dropping the indices for simplicity reasons, the system we solve can be resumed as :

$$\sum_{i\in I_C} f_i = 1 \tag{14}$$

$$\partial_t f_i - \frac{1}{r}\partial_r(r\sigma\partial_r f_i) + \mathrm{div_r}(u_s f_i) + \frac{1}{r}\partial_r(r\vartheta_{i,r} f_i) = F_i \tag{15}$$

$$\partial_t c_j - \frac{1}{r}\partial_r(r\sigma_j\partial_r c_j) + \tilde{u}\cdot\nabla_\mathrm{r}\, c_j = G_j, \tag{16}$$

where the speed u_s and the active motion speed $\vartheta_{i,r}$ will be detailed below.

We note that longitudinal diffusion and chemotactic speed vanish, because the dimensional analysis reveals that these two terms are negligible in comparison with the longitudinal transport [**?**]. From a biological point of view, that is equivalent to the assumption that the bacteria are not able to swim against the longitudinal flow, but that their active motion capabilities allow them to move along the radial direction.

The active transport speed $\vartheta_{i,r}$ is given by :

$$\vartheta_{i,r} = \left(\sum_{j\in I_S\cup I_C} \lambda_{i,j}\Upsilon_j, 0\right) \tag{17}$$

where Υ_j is computed from the chemo-attractant map c_j with the explicit formula :

$$\Upsilon_j(r,z) = -\left(\frac{1}{r}\int_0^r s c_j(s,z)ds - \frac{r}{R^2}\int_0^R s c_j(s,z)ds\right). \tag{18}$$

The mixture speed $u_s = (u_{s,r}, u_{s,z})$, solution of the asymptotic version of the Stokes equation is given by the explicit formulas

$$u_{s,z} = -\frac{\Lambda(r,z)}{\kappa(z)}\left(R\int_0^z \sum_{i\in I_C}\gamma_{f_i}(R,y)dy - R^2 U_{z,in} + \frac{R^2}{2}U_{per}(z)\right) + U_{per}(z) \tag{19}$$

$$u_{s,r} = \left(-\frac{1}{r}\int_0^r s\partial_z u_{s,z}(s,z)ds - \sum_{i\in I_C} f_i \sum_{j\in I_C\cup I_S}\lambda_{i,j}\Upsilon_j(r,z)\right), \tag{20}$$

where

$$\Lambda(r,z) = \int_r^R \frac{s}{\mu(s,z)}ds, \quad \kappa(z) = \int_0^R s\Lambda(s,z)ds, \quad U_{z,in} = \frac{1}{R^2}\int_0^R s\sum_{i\in I_C}\gamma_{f_i}(s,0)ds.$$

We emphasize that the speed field keeps track of the key parameters of the fluid mechanics: the heterogeneity of the viscosity μ, the boundary conditions $\gamma_{f_i}(R,z)$ through the mucosa, the average intake $U_{z,in}$, the peristaltism U_{per}, and the bacterial radial swim through the term Υ. We also note that, taking

$u = u_s$ and $\nabla\Phi = \Upsilon$, the volume conservation constraint (8) is preserved by construction, avoiding numerical problems of mass conservation. This approximate model represents a huge reduction of the computational load, with a speed up of about 70, but gives accurate approximations of the initial model [**?**].

3.3 Numerical implementation.

We solve Eqs. (15)-(16) by a first-order time splitting method, coded in matlab (MathWorks, version R2016b) and ran on a linux architecture. The code sources can be found at https://forgemia.inra.fr/simon.labarthe/gut-microbiota.git. At each iteration, we use a finite volume scheme on a MAC grid, with explicit time integration for the transport term (inforcing the positivity of the solution with a CFL condition) and implicit scheme for the diffusion. The spatial operators are applied alternatively in each spatial direction, wich reduces the size of the linear systems to be solved. We end the time loop by integrating the source term with a semi-implicit Euler method that preserves the positivity. Namelly, the negative contributions of the source function are passed on the left hand side and solved implicitly, while the positive contribution are kept in the right-hand side [**?**]. The implicitation of the negative term does not involve any linear system inversion: due to the multilinear form of the different terms of the source function, the matrix to be inverted is diagonal.

We note that we take advantage of the equation $\sum_{i\in I_C} f_i = 1$ to avoid solving the equation on c by taking $c = 1 - \sum_{i\in I_C, i\neq c} f_i$.

The model parameters can be found in Table 1 for the parameters related to diffusion, speed and initial conditions, in Table 3 for the parameters of the source function and in Table 4 for the boundary conditions.

3.4 Strategy of the numerical experiments.

To colonize the colon, the microbial populations have to face the flow of the intestinal content. Several mechanisms have been identified as putative drivers of the microbial populations spatial distribution[**?**]: 1) the polysaccharide level can shape the overall microbial population 2) the mucus zone can provide nutrients and protect the microbial populations from the luminal flow, 3) bacterial active swim may favour bacterial persistence, 4) epithelial motility, through peristaltism or segmentation contraction, can slow down the flow and help maintaining the microbes in the gut. In order to separate the different mechanisms, we first define a basal reference condition for comparisons: we knock down the peristaltism and the chemotactic activity, and select a polysaccharide input ($20\mathrm{g\,day^{-1}}$) representative of a normal reference diet.We then perform a long time simulation, starting from $f_m = f_{init,m}$, $f_l = 1 - f_m$ and $f_i = 0$, for all $i \in I_C$, $i \neq l, m$. The mucus initial condition $f_{init,m}$ is given by a sigmoid function, following [**?**], that distributes the mucus level from $f_{min_{init},m} := 0$ in the lumen to $f_{max_{init},m}$, the physiological amount of mucins in the mucus layer. We set

$$f_m(0,r,z) := f_{init,m} = f_{max_{init},m} + (f_{max_{init},m} - f_{min_{init},m}) \frac{r^{2\lambda_{m,init}}}{r^{2\lambda_{m,init}} + r_m^{2\lambda_{m,init}}}$$

where r_m is a threshold defining the average thickness of the mucus layer. This simulation is conducted until steady state, that is further used as a reference

state. We check that this reference state can be taken as a proxy of a healthy gut microbiota, by verifying that key markers are recovered in a physiological range (see the Results section). It is the initial condition of the additional numerical experiments, that are conducted until a new steady state was reached. This final state is compared to the reference initial state to assess the outcome of the experiment.

We next check the impact of the four putative mechanisms separately, by modifying only the model parameter that corresponds to the given mechanism. The effect of dietary fibre is assessed by increasing or decreasing the fibre intake by 30%. The effect of the mucus zone is checked in two different ways: in order to test if the nutrients provided by the mucus layer strongly shape the microbiota, we first knock down the mucus metabolism in the $\mathbf{B}_{mon}$ population by setting the consumption rate parameter to zero. As the mucus layer strongly impact the local rheology, we next remove the viscosity heterogeneity by taking a homogeneous viscosity map $\mu = 35 \times 10^3 \mathrm{g\,cm^{-1}\,day^{-1}}$, in order to check if the rheology discrepancies in the gut had an effect on the spatial repartition. The chemotactic function is introduced by setting $\lambda = 1/Grad_{max,j} \mathrm{cm^2\,day^{-1}}$ where $Grad_{max,j}$ is the maximal value of the gradient of the chemotactic potential of the chemoattractant j in the reference simulation, so that the characteristic value of the chemotactic speed is 1, small under the characteristic value of the longitudinal speed. The peristaltism is checked by setting $U_{per,r} = 0$ and $U_{per,z} = -10$ for $5 < z < 155$cm. The peristaltism is turned off near the boundaries $z = 0$ and $z = L$ in order to preserve the consistency of the boundary conditions.

The other parameters used in the simulations can be found in Tables 1, 3 and 4.

3.5 Sensitivity analysis.

We performed a local sensitivity analysis of the model output to parameter variations around the parameters identified in the previous simulations. We aimed at testing the impact of selected parameters on the bacterial distribution. Namely, we selected the gut motility ($U_{per,z}$ parameter), the bacterial chemotaxis (λ_{ij} parameter), the viscosity gradient ($\mu_{max,m}$ and $\mu_{max,l}$ parameters, that were shifted at the same time) and the fibre intake ($f_{pol,in}$ parameter). We studied the variations of the output $B(z) := \sum_{i \in I_B} \frac{2}{R^2} \int_0^R r c_i(r,z) dr$ when varying the selected parameters. We built a total factorial design by allowing for each parameter θ five levels corresponding to 50, 80, 100, 120 and 150% of its nominal value θ_0 introduced in Tables 1, 3 and 4. Testing 4 parameters resulted in a design containing 625 different sets of parameter values and the same number of model runs to perform the sensitivity analysis. The models outputs were post-processed with the R package Multisensi (https://CRAN.R-project.org/package=multisensi). We computed with Multisensi the descriptive statistics on $B(z)$, the distribution of the first order Sobol index of each parameters along the gut length with the method introduced in [**?**], and the Fig 14. We recall that for a given parameter θ, the first order Sobol index $S_\theta(z)$ of a given parameter θ and for a given $z \in (0, L)$ reads

$$S_\theta(z) := \frac{Var(\mathbb{E}(B(z)|\theta))}{Var(B(z))}.$$

4 Discussion

4.1 Modelling the gut microbiota in its environment

Several models of the gut microbiota were proposed in the literature to study the spatial structure of the microbial communities. The present model couples several modelling frameworks that were previously introduced: it adapts the metabolic model presented in [**?**] to the fluid mechanics model of the mucus and the gut content defined in [**?**], while taking into account hydrodynamics balances that were thoroughly studied in [**?**]. Our spatialization strategy can be compared to the method presented in [**?**], which was a unidimensional spatialization of [**?**], but we went deeper into details in the description of the fluid dynamics of the gut content and we also considered 3D phenomena that can occurs in the radial direction of the gut. To our knowledge, the present study introduces the first model that consider the interactions of the gut microbiota with its fluid environment by explicitly coupling a population dynamic model of the microbiota and the key luminal metabolites to a fluid dynamic model of the intestinal flow. This modelling platform is a suitable framework to study the spatial structure of the microbiota and the interactions of the bacterial populations with their environment.

4.2 Model improvements

Several limitations of our approach can be underlined. First, the description of the bacterial metabolic activity is reduced to a compact version of the fibre degradation pathways leading from carbohydrates to the main end products: lactate, SCFA and gas. This model is built from prior knowledge of fibre degradation and focuses on the metabolism of the main source of substrate in the gut: carbohydrates. But it neglects other secondary processes. Other metabolic activities are activated, such as bile acid degradation or iron sequestration, that could have a significant importance in the spatial structure of the bacterial populations. Some important abiotic parameters were neglected, such as the redox balance or the complex acido-basic reactions that modify the pH. If needed for a specific study, the metabolic pathways of our model can be supplemented by additional processes of interest, in a case-by-case basis.

Secondly, several biophysical mechanisms of spatial structuration were ruled out. To face the luminal flow, the bacterial communities can express specific phenotypes. Bacterial aggregation or chains formation may be a collective behaviour that was selected for enhancing the friction forces and increasing the retention times in the gut. Several bacteria are also able to bind to materials trapped in the mucus layer, such as DNA strands or lysate residuals: this ability allows them to grow near the carbohydrates incorporated in the mucus which gives them a competitive advantage. Those behaviours were not modelled in this study, but can be addressed with classical aggregation models such as Smoluchowski equations, or by adding additional friction terms in the moment conservation equation (10).

Finally, if the outputs of the reference model are in the range of observed data, some differences remain: the simulated total microbiota mass at the gut end is half the observation in feces but the simulated total number of bacteria is twice the experimental measures. These discrepancies may reflect the impor-

tant simplifications that we used in modelling the microbiota. From a metabolic point of view, focusing on fibre metabolism only would lead to underestimate bacterial growth and consequently the overall bacterial levels. Moreover, we do not model the final part of the colon but the gut content desiccation through water absorption is still active in the sigmoid compartment, which mechanically increases the microbial concentration. This mechanism could account for the discrepancies between our numerical prediction at the gut end and the measured bacterial concentration in faeces. Furthermore, the bacterial phases are considered in our model as a homogeneous mixture of liquid and bacteria that form at a macroscopic scale a viscous fluid: the derivation of bacterial densities expressed in $\mathrm{g\,cm^{-3}}$ or $CFU.g^{-1}$ then relies on assumptions on the average bacterial volume or on the volume saturation by the bacteria in the bacterial phase, which are questionable when modelling bacterial communities with diverse individual shapes and volumes. These modelling issues could be addressed by developing microscale models of the bacterial communities that could be upscaled through mathematical methods such as homogeneization in order to better control those approximations.

4.3 Suitable data for model assessment

Linking outputs of spatial models of the gut microbiota to experimental data for assessment or inference purpose is challenging, due to the gap that still remains between the modelled entities and the biological observations. Omics data can be produced from stool samples, reflecting the state of the gut system at its end: metagenomic data give an insight in the microbial composition of the microbiota and in its functional potential. Metatranscriptomics and metabolomics provide information on the effective expression of microbial functions. In the present study, we could compare levels of specific metabolites, such as SCFA, to measurements in different gut compartments, or overall bacterial levels. But we have no way to directly link the bacterial levels predicted by our model to metagenomic data, because the modeled bacterial densities are not indexed to any counts of genomic markers. It would be necessary to provide a set of marker genes associated to the different functional population involved in our model. Those marker genes could be a set of $16s$ genes detailling the taxonomic composition of the functional populations that could be compared to $16s$ counts from stool samples. They could also be a set of genes characterizing the metabolic functions of the functional populations, that could be compared to the corresponding gene counts in shotgun metagenomic data.

Assessing experimentally the spatial structure of the microbiota implies the production of spatial images of the microbial and metabolite distribution. An experimental setup was recently developed [**?**] in order to track the spatio-temporal evolution of a simplified microbiota of 15 bacterial strains, labelled with a different dye for imaging purpose, and covering the main part of the functions observed in a healthy microbiota. This kind of data set is very promising for assessing spatio-temporal model of the gut microbiota. However, it would need again to modify the structure of the model in order to fit with the specific bacterial populations involved in the experimental study.

4.4 Effective drivers of the spatial structure of the gut microbiota

In [?], the balance between bacterial growth and bacterial dilution by the convection was carefully studied, in order to identify a range of gut content flow allowing bacterial colonization. The author argued that the hydrodynamics alone was not sufficient to reduce the apparent speed in the gut under the dilution threshold, which is a necessary condition for bacterial growth. Several biological mechanisms capable to enforcing the speed reduction or enhancing the retention time were thoroughly discussed and peristaltism was identified as the preponderant mechanism that supplements the hydrodynamics to enable the settlement of bacterial communities.

In the present study, additional fluid mechanic effects were introduced, such as viscosity heterogeneities that provide low speed zones near the gut resulting in the creation of favourable niches in the mucosa vicinity where the local dilution rate is lower than the bacterial growth. We emphasize that such favourable zones were recently observed by imaging a simplified microbiota composed of 15 labelled bacterial strains: high bacterial concentrations were observed in the surroundings of the mucosal wall, but outside the outer mucus layer [?]. Viscosity heterogeneities in themselves were sufficient to supplement the basal hydrodynamics in order to make bacterial colonization possible. Additional effects, such as gut motility or bacterial active swimming, counter-balance the dilution by the fluid flow and consolidate the bacterial levels in the gut. We then identified a multifactorial process that include fluid rheology, peristaltism and active swimming, that lead to the constitution of ecological niches in the fluid gut environment. However, the sensitivity analysis of our model identified the fibre input as the main driver of the microbiota spatial structure, except in the proximal part, where the epithelial motility is determinant for the colonization of the proximal gut. The variations of viscosity gradients weakly impact the bacterial distribution, but an homogeneous viscosity drastically drops down the bacterial populations. This indicates that viscosity heterogeneity is constitutive of a physiological level of bacterial populations, but that the magnitude of these heterogeneities is not preponderant comparatively to the other processes. Threshold effects in the viscosity map near the mucus layer could be the main ingredient of this observation.

Active swimming is often discarded as a possible mechanism enhancing bacterial colonization in the gut, with the arguments that 1) metaproteomic screening of the gut microbiota showed that flagella expression achieved very low levels [?], 2) the maximal known active swimming speeds are in the same order of magnitude than the luminal longitudinal fluid flow, meaning that the bacteria should continuously swim at their maximal capability in order to counter-balance the luminal streams [?], 3) the flagellin is targeted by the host immune system near the epithelium [?]. However, our model showed that very low active swimming (with velocities two orders of magnitude under the longitudinal flow of gut content) is enough to noticeably enhance the bacterial levels in the gut. The active swimming is not used to directly face the strong longitudinal streams, since the chemotactic transport in the longitudinal direction is neglected in our model, but to reach the favourable niches near the mucosa.

5 Conclusion

We introduced a continuous spatio-temporal model of the gut microbiota, that couples a population dynamics model of functional population involved in a trophic chain related to fiber degradation to a fluid mechanic model of the gut content. A mathematical simplification allowed to reduce the computation time by a factor 70 while keeping the main features. This model was used to investigate the mechanisms driving the spatial distribution of the gut content and of the microbial populations in the colon. We tested the relative impact of epithelial motility, bacterial active swimming and diet variations through a sensitivity analysis of our model, identifying the later as the preponderant driver of the spatial structure except in the proximal colon where peristaltism is the main effect. We observed that very low active swimming capabilities are enough to favour the bacterial growth, indicating that this mechanism should not be discarded from spatial studies of the gut microbiota. We furthermore exhibited a new mechanism involved in bacterial persistence in the gut, based on radial gradients of viscosity that induce the creation of slow stream zones near the mucosa that can be considered as favourable spatial niches in the vicinity of the mucus layer.

Acknowledgments

This publication has been written with the support of the AgreenSkills+ fellowship programme which has received funding from the EU's Seventh Framework Programme under grant agreement Number FP7-609398 (AgreenSkills+ contract).

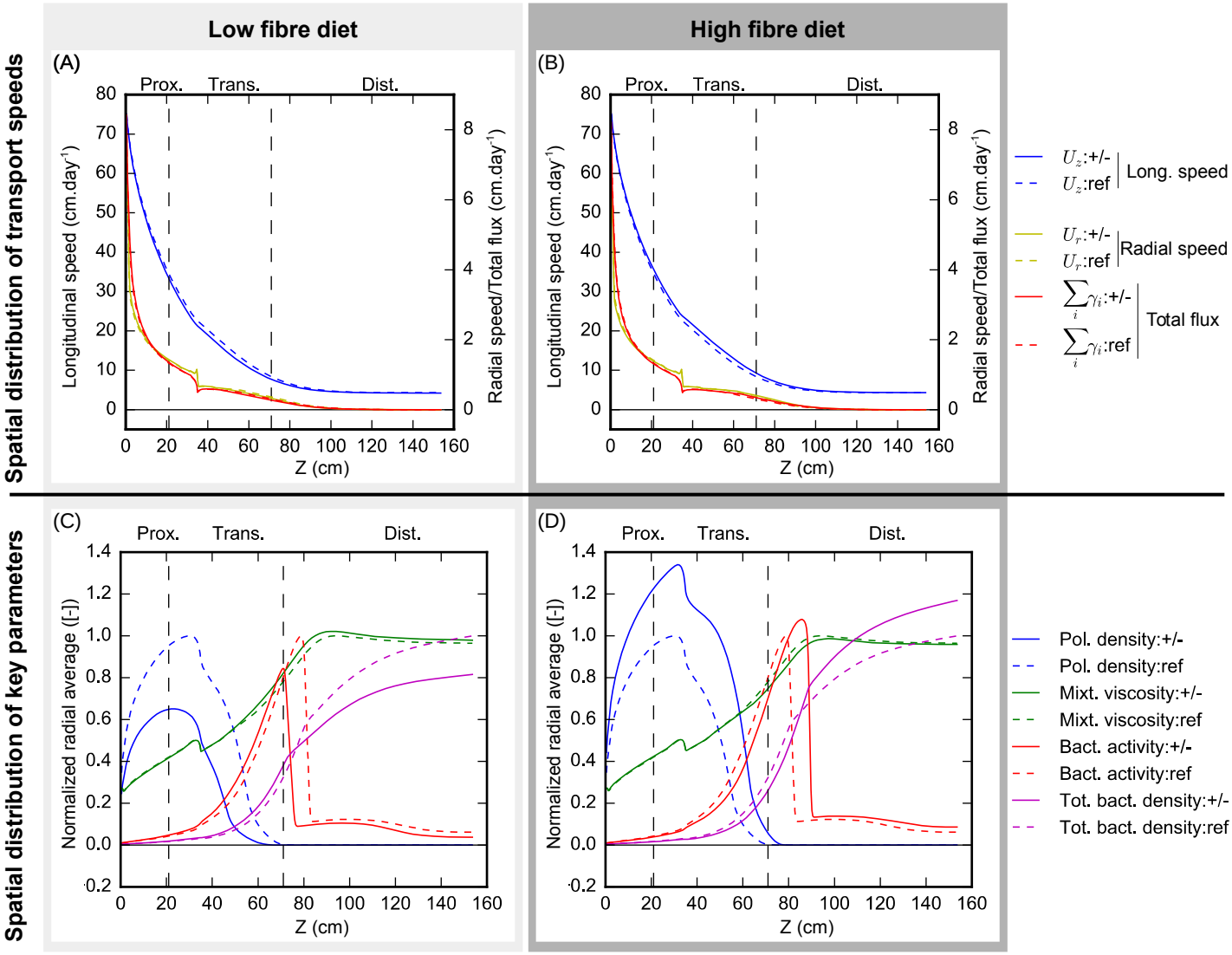

Figure 7: **Impact of the diet on the transport speeds and on the spatial structure.** We reproduce the quantities of Fig. 3, with a low-fibre diet (30% decrease of polysaccharide input, (A) and (C)) and high-fibre diet (30% increase, (B) and (D)), that we compare with the reference fibre diet (same polysaccharide input, dashed lines). In the upper panels (A) and (B), the speed distribution is reproduced, whereas the lower panels (C) and (D) display the spatial distribution of relevant parameters: all the values are normalized respectively to the maximal values of the reference diet (see Fig 3 for nominal values). Higher fibre diet enhances the transit speed, the fibre concentration, the bacterial activity and the microbial levels, while slightly locally reducing the viscosity. Less fibre lead to an opposite effect.

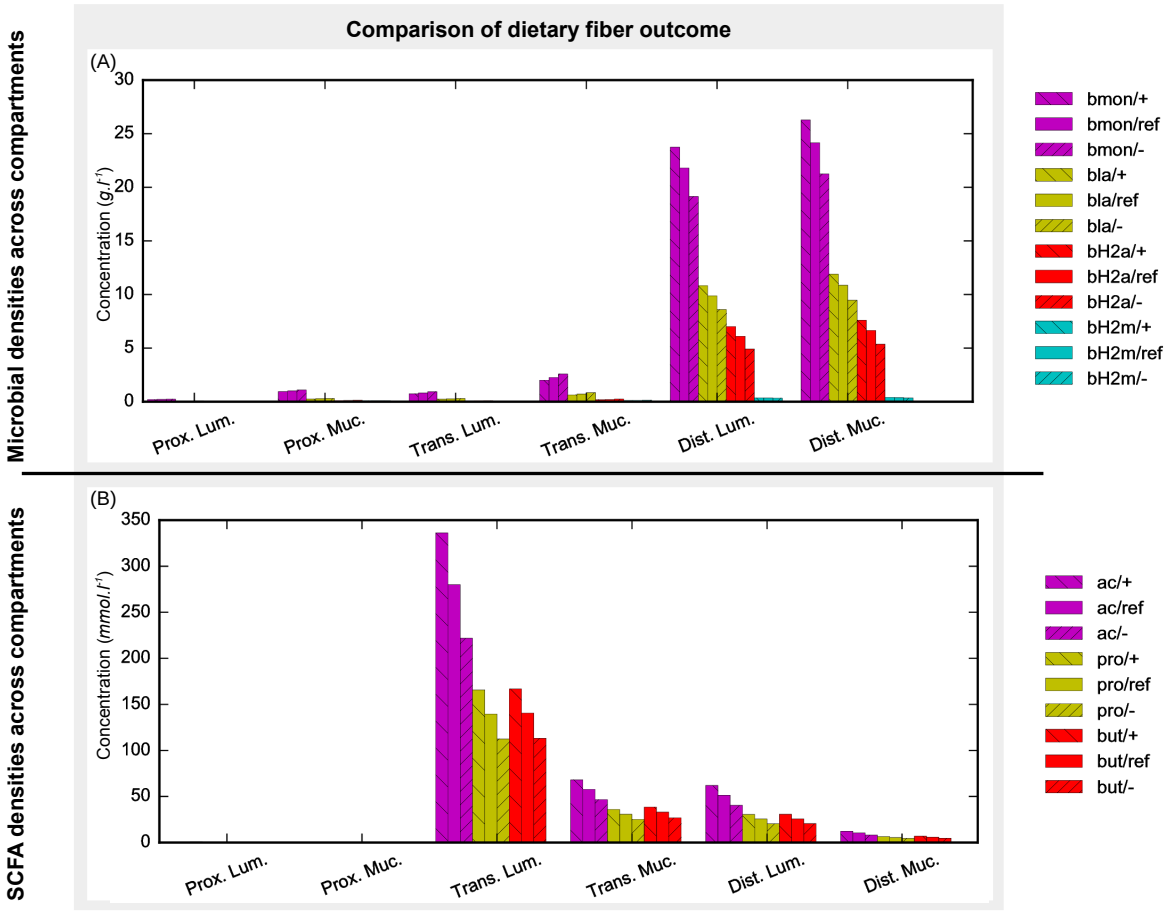

Figure 8: Microbial and SCFA levels in the different compartments. We compare the microbial (A) and SCFA (B) levels during high-fibre(30% increase of polysaccharide input, reverse slash hatches) or low-fibre (30% decrease, slash hatches) diets with reference levels during normal diet (same polysaccharide input, plain boxes). The bacterial and SCFA levels are directly related to the fibre intake.

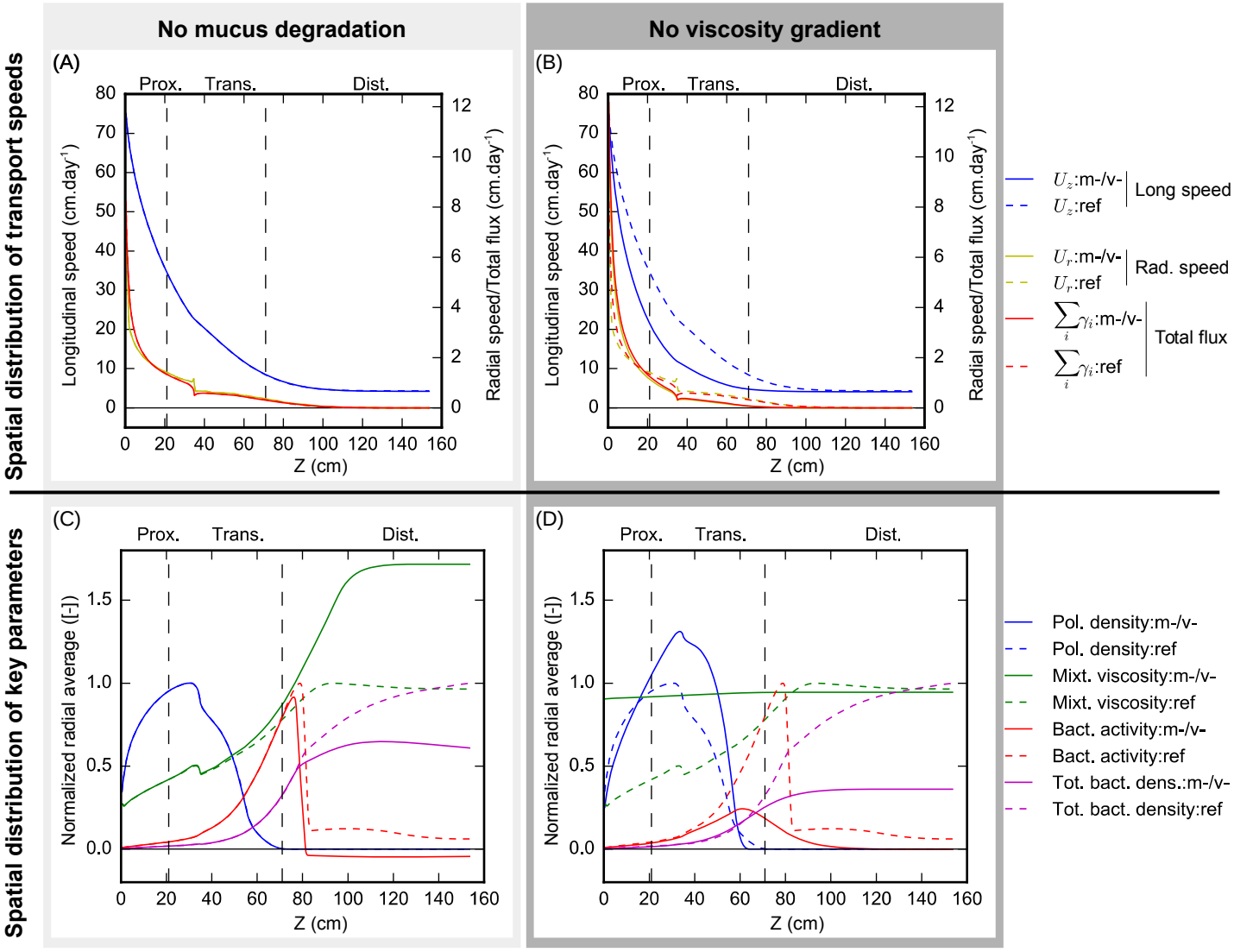

Figure 9: **Impact of viscosity and mucus degradation on the outcome of the model.** We reproduce the quantities of Fig. 3 with no mucus degradation ($m-$, A and C) or with a homogeneous viscosity ($v-$, B and D), compared with the reference-fibre diet of Fig. 3 (ref, dashed lines). All the values are normalized respectively to the maximal values of the reference. The mucus degradation has an effect in the distal bowel only. A homogeneous viscosity has a deep impact on the bacterial activity and the microbial levels.

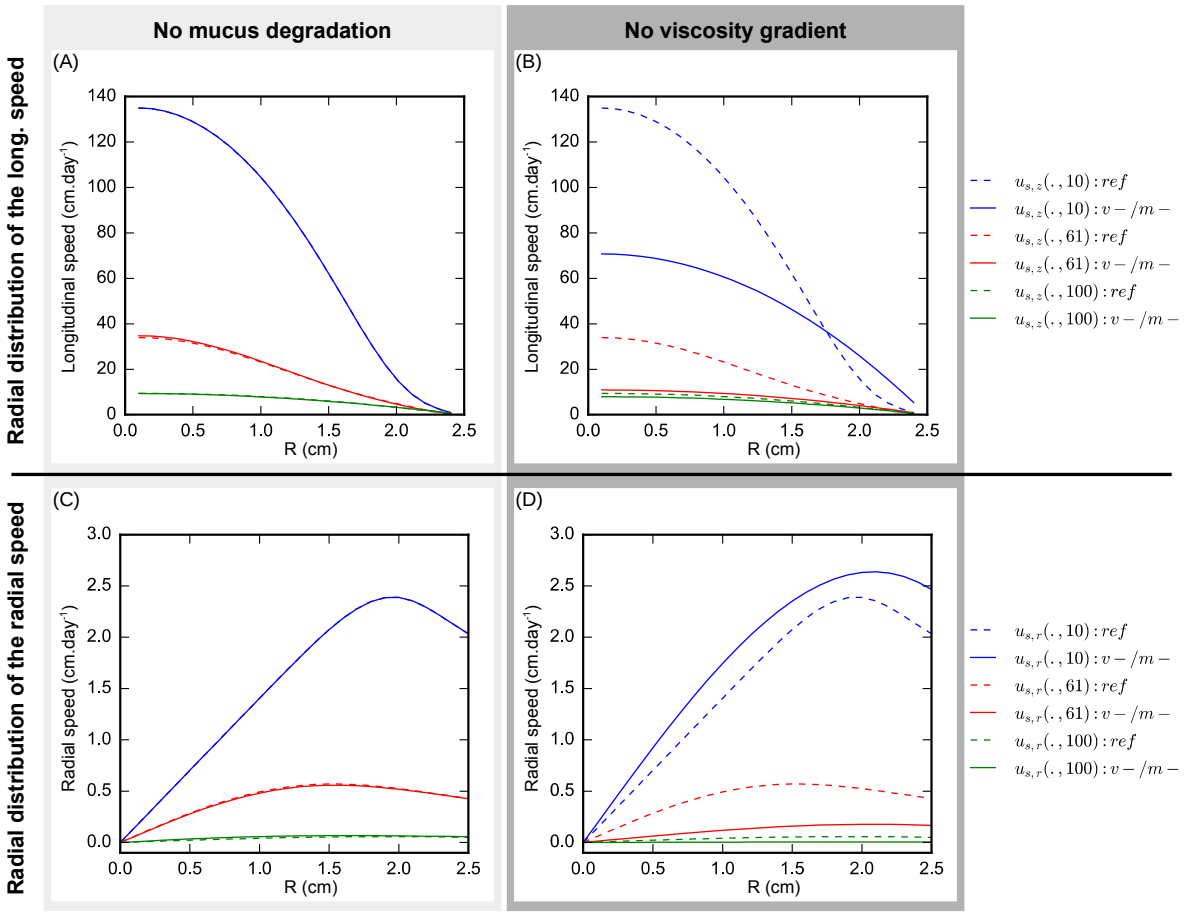

Figure 10: Radial distribution of the longitudinal ($u_{s,z}$) and radial ($u_{s,r}$) speeds at $z = 10$, 61, and 100cm. To further explore the drivers of the bacterial activity, we display the radial distribution of the speed components at different lengths with no mucus degradation ($m-$, A and C) or a homogeneous viscosity ($v-$, B and D), compared with the reference of Fig. 3 (ref, dashed lines).

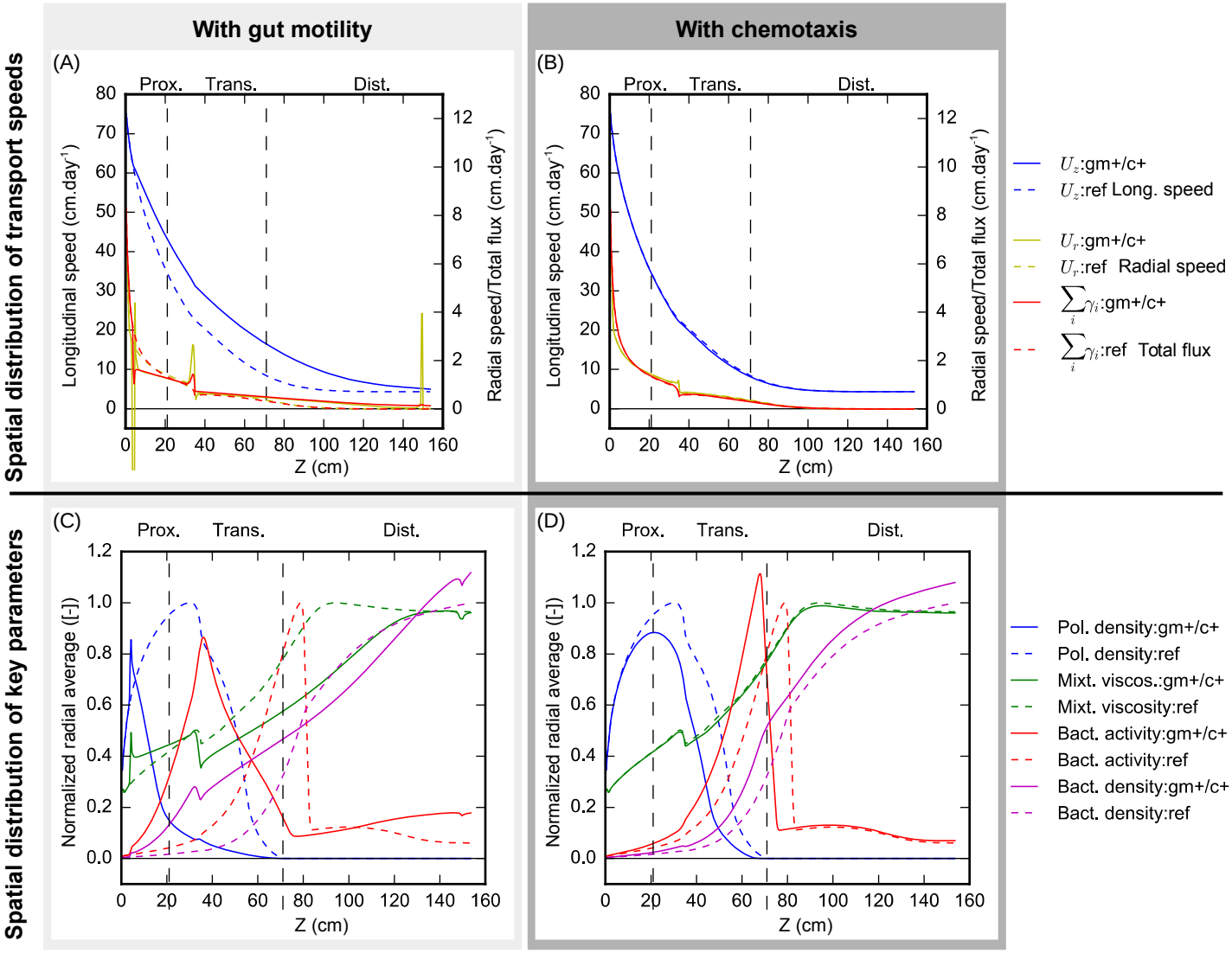

Figure 11: **Impact of peristaltism and chemotaxis on the outcome of the model**. We reproduce the quantities of Fig. 3 with gut motile activity ($gm+$, A and C) or chemotactic active swimming ($c+$, B and D), compared with the reference-fibre diet of Fig. 3 (ref, dashed lines). All the values are normalized respectively to the maximal values of the reference. The gut motility shifts proximally the bacterial activity, enhancing the bacterial levels in the proximal and transverse gut, while reducing the viscosity. The bacterial active motion promotes an earlier colonization of the gut, resulting in increasing proximally the metabolic activity and the microbial concentrations.

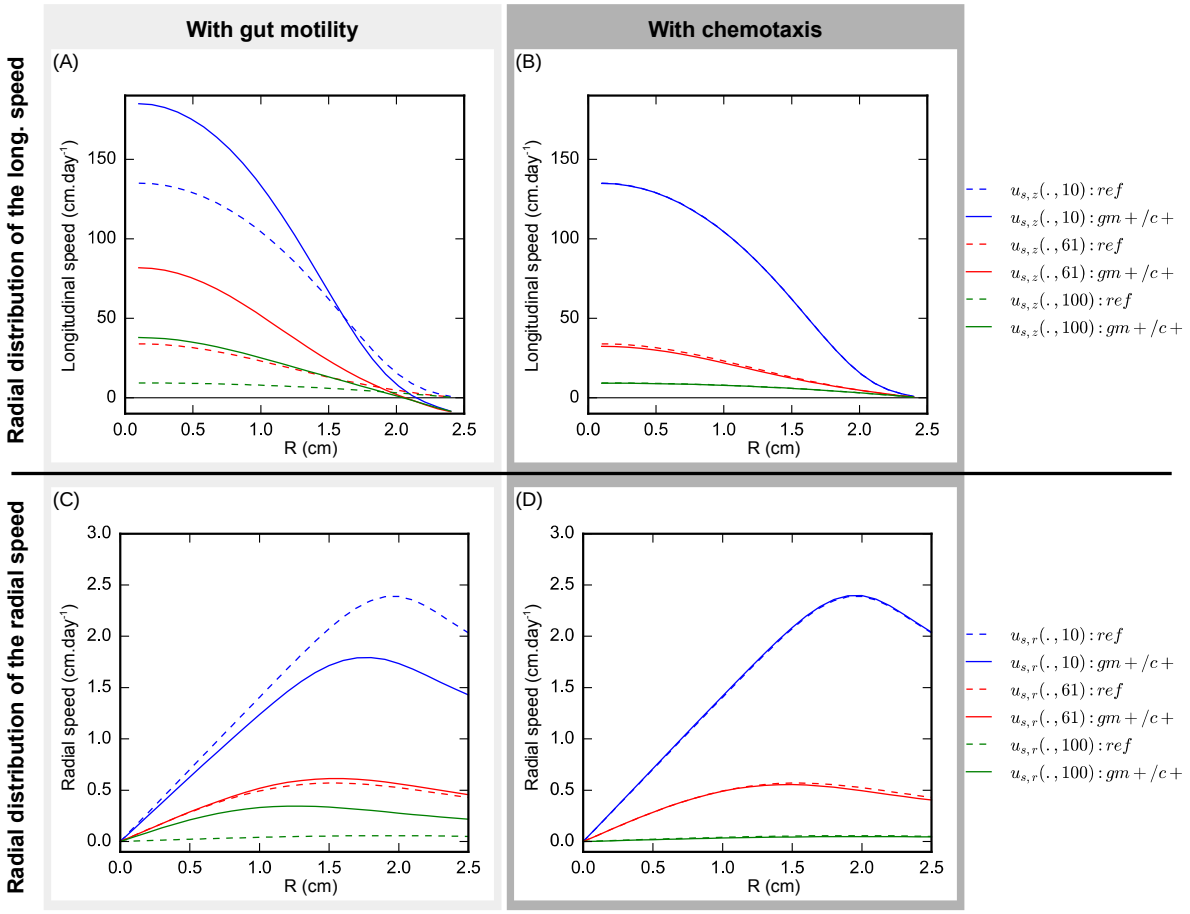

Figure 12: Radial distribution of the longitudinal and radial speeds at $z = 10$, 61, and 100cm. To assess the effect of peristaltism and chemotaxis on the spatial structure of intestinal hydrodynamics, we display the radial distribution of the speed components at different lengths with gut motility ($gm+$, A and C) or bacterial chemotaxis ($c+$, B and D), compared with the reference of Fig. 3 (ref, dashed lines).

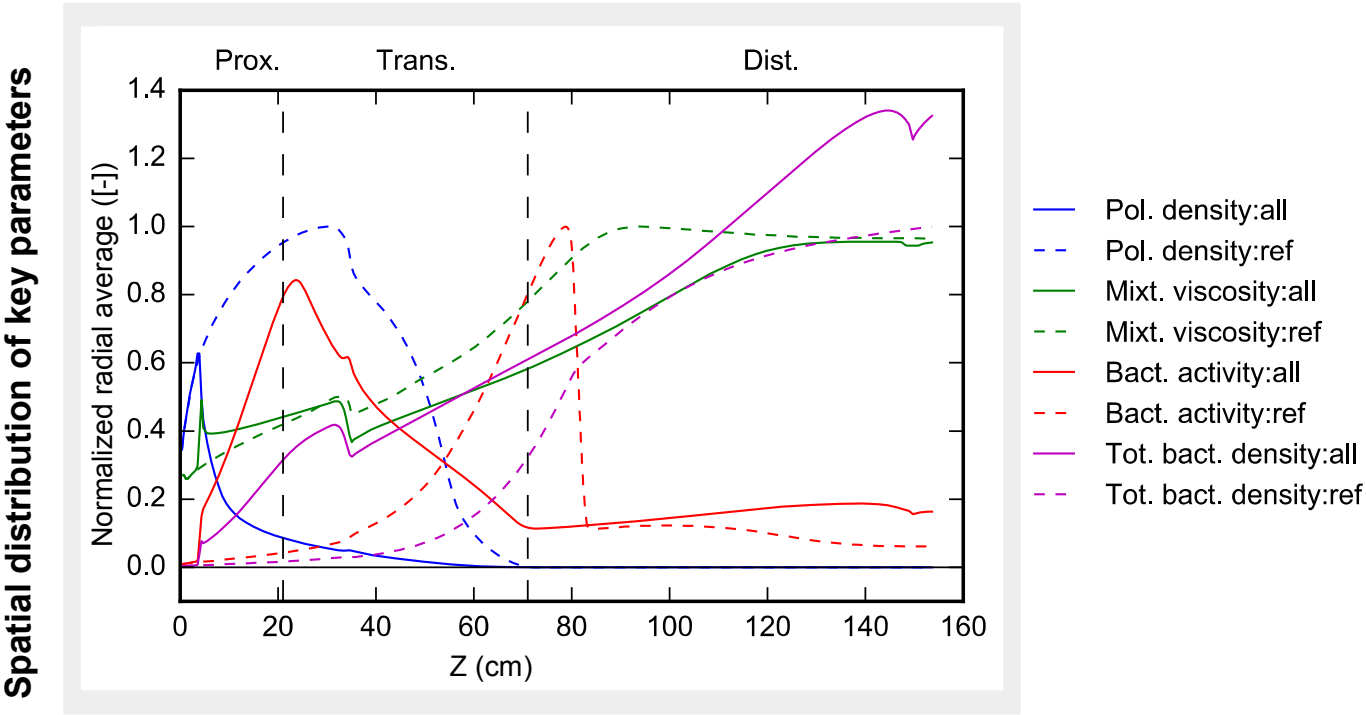

Figure 13: **Longitudinal distribution of the averaged key parameters when all the mechanisms are combined.** We investigate the impact of the combination of all the impacts on the outcome of the model. We reproduce in (a) the quantities of Fig. 3 with all the mechanisms, i.e. peristaltism, viscosity gradients and chemotaxis (*all*, circle lines), compared with the reference-fibre diet of Fig. 3 (ref, dashed lines). All the values are normalized respectively to the maximal values of the reference. The metabolic activity and the bacterial levels are boosted when all the mechanisms are combined.

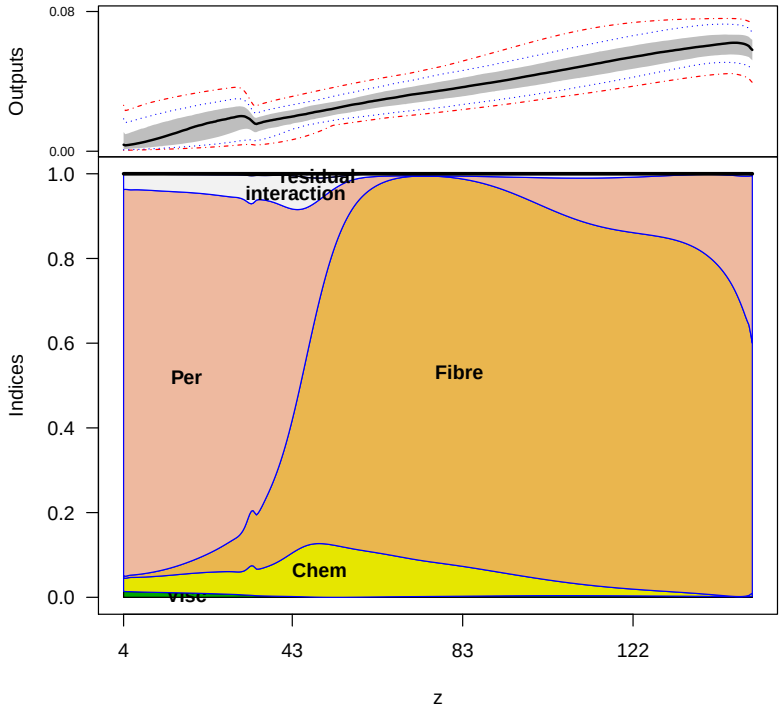

Figure 14: **Longitudinal distribution of the first order Sobol index.** We perform a global sensitivity analysis to assess the impact of the parameters driving the peristaltism, the fibre input, the mixture viscosity and the chemotaxis magnitude on the longitudinal distribution of the radially averaged bacterial populations (i.e. on $B(z) := \sum_{i \in I_B} \frac{2}{R^2} \int_0^R r c_i(z,r) dr$, where I_B is the set of bacterial populations and c_i the different bacterial levels). For each z in $(0, L)$, the upper plot displays the dispersion of $B(z)$ when sampling the parameter space by indicating the extremal values (red dashed lines), the first and last deciles (blue dot lines), the second and third quartiles (gray zones) and the median value (black bold line). The lower panel displays for each z the first order Sobol index of each parameter, i.e. the part of the total output variance explained by a given parameter. Per: peristaltism magnitude, Fibre: level of fibre input, Chem: magnitude of the chemotactic activity, Visc: mixture viscosity. Interaction: second order Sobol Index. Residual: residual in the total variance decomposition. The gut motility is preponderant in the proximal part, while fibre levels is the main driver of the bacterial levels in the transverse and distal compartments.

Source Function				
Parameter	Value	Unit	Description	Ref.
α	0.113	$\mathrm{cm^3\,mol^{-1}}$	Multiplicative constant for unit conversion	
k_{P1}	1.20e3	$\mathrm{d^{-1}}$	Maximum specific reaction rate for P1	[?]
k_{P2}	1.20e3	$\mathrm{d^{-1}}$	Maximum specific reaction rate for P2	[?]
k_{P3}	7.92	$\mathrm{d^{-1}}$	Maximum specific reaction rate for P3	[?]
k_{P4}	103	$\mathrm{d^{-1}}$	Maximum specific reaction rate for P4	[?]
k_{P5}	108.837	$\mathrm{d^{-1}}$	Maximum specific reaction rate for P5	[?]
k_{P6}	22.581	$\mathrm{d^{-1}}$	Maximum specific reaction rate for P6	[?]
k_{P7}	0.01	$\mathrm{d^{-1}}$	Maximum specific reaction rate for P7	[?]
k_{P8}	0.01	$\mathrm{d^{-1}}$	Maximum specific reaction rate for P8	[?]
k_{P9}	0.01	$\mathrm{d^{-1}}$	Maximum specific reaction rate for P9	[?]
k_{P10}	0.01	$\mathrm{d^{-1}}$	Maximum specific reaction rate for P10	[?]
k_{P11}	200	$\mathrm{d^{-1}}$	Maximum specific reaction rate for P11	[?]
k_{P12}	200	$\mathrm{d^{-1}}$	Maximum specific reaction rate for P12	[?]
k_{P13}	200	$\mathrm{d^{-1}}$	Maximum specific reaction rate for P13	[?]
$K_{h,P11}$	0.0011	$\mathrm{mol\,bar^{-1}}$	Henry's Law coefficient	[?]
$K_{h,P12}$	0.0255	$\mathrm{mol\,bar^{-1}}$	Henry's Law coefficient	[?]
$K_{h,P13}$	7.29e-4	$\mathrm{mol\,bar^{-1}}$	Henry's Law coefficient	[?]
R	0.08314	$\mathrm{bar\,mol^{-1}\,K^{-1}}$	Ideal gas constant	[?]
T	310.15	K	Gut absolute temperature	[?]
$[CH_{4,g}]_\infty$	$1.9106e-10$	$\mathrm{mol\,cm^{-3}}$	Gaseous CH_4 steady state level	[?]
$[C0_{2,g}]_\infty$	$1.19e-5$	$\mathrm{mol\,cm^{-3}}$	Gaseous CO_2 steady state level	[?]
$[H_{2,g}]_\infty$	$3.6505e-7$	$\mathrm{mol\,cm^{-3}}$	Gaseous H_2 steady state level	[?]
$K_{x,P1}$	20.265	[-]	Half saturation constant (Comtois law) [-]	[?]
$K_{x,P2}$	0.265	[-]	Half saturation constant (Comtois law) [-]	[?]
$K_{s,P3}$	$2.6e-6$	$\mathrm{mol\,cm^{-3}}$	Half saturation for Monod law	[?]
$K_{s,P4}$	$6.626e-6$	$\mathrm{mol\,cm^{-3}}$	Half saturation for Monod law	[?]
$K_{s,P5}$	$1.7e-6$	$\mathrm{mol\,cm^{-3}}$	Half saturation for Monod law	[?]
$K_{s,P6}$	$1.563e-9$	$\mathrm{mol\,cm^{-3}}$	Half saturation for Monod law	[?]
$Y_{m,P1}$	$8.850e-3$	[-]	Yield of component m in process 1,	[?]
$Y_{mon,P1}$	$4.425e-5$	[-]	Yield of component mon in process 1,	[?]
$Y_{pol,P2}$	$8.850e-3$	[-]	Yield of component pol in process 2,	[?]
$Y_{mon,P2}$	$4.425e-5$	[-]	Yield of component mon in process 2,	[?]
$Y_{mon,P3}$	$8.850e-3$	[-]	Yield of component mon in process 3,	[?]
$Y_{\mathbf{B}_{mon},P3}$	0.120	[-]	biomass yield factor for $\mathbf{B}_{mon}$,	[?]
$Y_{la,P3}$	$4.416e-3$	[-]	Yield of component la in process 3,	[?]
$Y_{ac,P3}$	$5.18e-3$	[-]	Yield of component ac in process 3,	[?]
$Y_{pro,P3}$	$2.124e-3$	[-]	Yield of component pro in process 3,	[?]
$Y_{but,P3}$	$2.389e-3$	[-]	Yield of component but in process 3,	[?]
$Y_{CO_2,P3}$	$9.735e-3$	[-]	Yield of component CO2 in process 3,	[?]
$Y_{H_2,P3}$	$1.274e-2$	[-]	Yield of component H2 in process 3,	[?]
$Y_{la,P4}$	$8.850e-3$	[-]	Yield of component la in process 4,	[?]
$Y_{\mathbf{B}_{la},P4}$	0.120	[-]	biomass yield factor for $\mathbf{B}_{la}$,	[?]
$Y_{ac,P4}$	$1.177e-3$	[-]	Yield of component ac in process 4,	[?]
$Y_{pro,P4}$	$2.363e-3$	[-]	Yield of component pro in process 4,	[?]
$Y_{but,P4}$	$1.770e-3$	[-]	Yield of component but in process 4,	[?]
$Y_{CO_2,P4}$	$4.717e-3$	[-]	Yield of component CO2 in process 4,	[?]
$Y_{H_2,P4}$	$3.540e-3$	[-]	Yield of component H2 in process 4,	[?]
$Y_{H_2,P5}$	$8.850e-3$	[-]	Yield of component H2 in process 5,	[?]
$Y_{\mathbf{B}_{H_2,a},P5}$	0.043	[-]	biomass yield factor for $\mathbf{B}_{H_2,a}$,	[?]
$Y_{ac,P5}$	$1.265e-3$	[-]	Yield of component ac in process 5,	[?]
$Y_{CO_2,P5}$	$-4.424e-3$	[-]	Yield of component CO2 in process 5,	[?]
$Y_{H_2,P6}$	$8.850e-3$	[-]	Yield of component H2 in process 6,	[?]
$Y_{\mathbf{B}_{H_2,m},P6}$	0.062	[-]	biomass yield factor for $\mathbf{B}_{H_2,m}$,	[?]
$Y_{CH_4,P6}$	$8.407e-4$	[-]	Yield of component CH4 in process 6,	[?]
$Y_{CO_2,P6}$	$-3.982e-3$	[-]	Yield of component CO2 in process 6,	[?]
$I_{Ph_{min}}$	5.5	[-]	Ph in the proximal part of the gut	[?]
$I_{Ph_{max}}$	6.8	[-]	Ph in the distal part of the gut	[?]
$I_{Ph_{low}}$	5.8	[-]	Threshold of inhibition	[?]
$I_{Ph_{high}}$	6.7	[-]	Threshold of inhibition	[?]

Table 3: Parameter values of the source function

Input fluxes on Γ_{in}				
Parameter	Value	Unit	Description	Ref.
$u_{z,in}$	$1.5 * 10^3/(2\pi R^2)$	$\mathrm{cm\,d^{-1}}$	Half average surface inflow	[?]
$f_{m,in}$	$f_m(0,r,z)$	$[-]$	Mucus density input	[?]
$f_{\mathbf{B}_{mon},in}$	$6.1e-5$	$[-]$	Dietary b_{mon} input	[?]
$f_{\mathbf{B}_{la},in}$	$2.03e-5$	$[-]$	Dietary b_{la} density input	[?]
$f_{\mathbf{B}_{h2a},in}$	$1.01e-5$	$[-]$	Dietary b_{h2a} density input	[?]
$f_{\mathbf{B}_{h2m},in}$	$1.01e-5$	$[-]$	Dietary b_{h2m} density input	[?]
$f_{pol,in}$	$1.33e-2$ (i.e. $25\mathrm{g\,d^{-1}}$)	$[-]$	Dietary polysac. density input	[?]
$c_{mon,in}$	$3.33e-5$	$\mathrm{mol\,cm^{-3}}$	Dietary monosac. density input	[?]
$c_{la,in}$	0	$\mathrm{mol\,cm^{-3}}$	Dietary lactate flow	[?]
$c_{ac,in}$	0	$\mathrm{mol\,cm^{-3}}$	Dietary acetate flow	[?]
$c_{bu,in}$	0	$\mathrm{mol\,cm^{-3}}$	Dietary butyrate flow	[?]
$c_{pro,in}$	0	$\mathrm{mol\,cm^{-3}}$	Dietary propionate flow	[?]
$c_{h2,in}$	0	$\mathrm{mol\,cm^{-3}}$	Dietary H_2 flow	[?]
$c_{ch4,in}$	0	$\mathrm{mol\,cm^{-3}}$	Dietary methane flow	[?]
$c_{co2,in}$	0	$\mathrm{mol\,cm^{-3}}$	Dietary CO_2 flow	[?]
Boundary conditions on Γ_m				
γ_m	3	$\mathrm{cm\,d^{-1}}$	Mucus production	[?]
$\gamma_{b_{mon}}$	0	$\mathrm{cm\,d^{-1}}$	Mucosal barrier for b_{mon}	[?]
$\gamma_{b_{la}}$	0	$\mathrm{cm\,d^{-1}}$	Mucosal barrier for b_{la}	[?]
$\gamma_{b_{h2a}}$	0	$\mathrm{cm\,d^{-1}}$	Mucosal barrier for b_{h2a}	[?]
$\gamma_{b_{h2m}}$	0	$\mathrm{cm\,d^{-1}}$	Mucosal barrier for b_{h2m}	[?]
$\gamma_{l,max}$	17	$\mathrm{cm\,d^{-1}}$	Proximal liquid uptake	-
$\gamma_{l,min}$	2	$\mathrm{cm\,d^{-1}}$	Distal liquid uptake	-
γ_{pol}	0	$\mathrm{cm\,d^{-1}}$	Mucosal polysaccharides flow	[?]
γ_{mon}	0	$\mathrm{cm\,d^{-1}}$	Mucosal monosaccharides flow	[?]
$\gamma_{la,max}^{(prox)}$	16.85	$\mathrm{cm\,d^{-1}}$	Proximal mucosal lactate flow	[?]
$\gamma_{la,min}^{(trans)}$	16.29	$\mathrm{cm\,d^{-1}}$	Transverse mucosal lactate flow	[?]
$\gamma_{ac,max}^{(prox)}$	25.28	$\mathrm{cm\,d^{-1}}$	Proximal mucosal acetate flow	[?]
$\gamma_{ac,min}^{(trans)}$	24.43	$\mathrm{cm\,d^{-1}}$	Transverse mucosal acetate flow	[?]
$\gamma_{bu,max}^{(prox)}$	17.23	$\mathrm{cm\,d^{-1}}$	Proximal mucosal butyrate flow	[?]
$\gamma_{bu,min}^{(trans)}$	16.81	$\mathrm{cm\,d^{-1}}$	Transverse mucosal butyrate flow	[?]
$\gamma_{pro,max}^{(prox)}$	20.49	$\mathrm{cm\,d^{-1}}$	Proximal mucosal propionate flow	[?]
$\gamma_{pro,min}^{(trans)}$	19.93	$\mathrm{cm\,d^{-1}}$	Transverse mucosal propionate flow	[?]
$\gamma_{m,h2}^{(prox)}$	0	$\mathrm{cm\,d^{-1}}$	Proximal mucosal H_2 flow	[?]
$\gamma_{m,ch4}^{(prox)}$	0	$\mathrm{cm\,d^{-1}}$	Proximal mucosalmethane flow	[?]
$\gamma_{m,co2}^{(prox)}$	0	$\mathrm{cm\,d^{-1}}$	Proximal mucosal CO_2 flow	[?]

Table 4: Parameters of the boundary fluxes.